PEDRO HENRIQUE BERNARDI FRANZINI

EXPERIMENTAL ANALYSIS OF THE FLOW AROUND AN AIRFOIL UNDER GROUND AND DOWNFORCE EFFECTS

UNIVERSIDADE FEDERAL DE UBERLÂNDIA

FACULDADE DE ENGENHARIA MECÂNICA

2022

PEDRO HENRIQUE BERNARDI FRANZINI

EXPERIMENTAL ANALYSIS OF A FLOW AROUND AN AIRFOIL UNDER THE EFFECT OF DOWNFORCE AND GROUND EFFECT

Undergraduate Thesis submitted to the Aeronautical Engineering Course of the Faculdade de Engenharia Mecânica of the Federal University of Uberlândia, as a partial requirement for obtaining the Bachelor Degree in Aeronautical Engineering.

Advisor: Prof. Dr. Odenir de Almeida

UBERLÂNDIA
2022

PEDRO HENRIQUE BERNARDI FRANZINI

EXPERIMENTAL ANALYSIS OF A FLOW AROUND AN AIRFOIL UNDER THE EFFECT OF DOWNFORCE AND GROUND EFFECT

Undergraduate Thesis submitted to the Aeronautical Engineering Course of the Faculdade de Engenharia Mecânica of the Federal University of Uberlândia, as a partial requirement for obtaining the Bachelor Degree in Aeronautical Engineering.

Approved on: 6th April 2022

EXAMINATION BOARD

Prof. Dr. Odenir de Almeida (Advisor)
Federal University of Uberlândia (UFU)

Prof. Dr. Giuliano Gardolinski Venson
Federal University of Uberlândia (UFU)

Prof. Dr. Daniel Dall'Onder dos Santos
Federal University of Uberlândia (UFU)

UNIVERSIDADE FEDERAL DE UBERLÂNDIA
Coordenação do Curso de Graduação em Engenharia Aeronáutica
Rodovia BR 050, KM 78, Bloco 1D, 2º andar - Bairro Glória, Uberlândia-MG, CEP 38400-902
Telefone: (34) 2512-6768 - www.mecanica.ufu.br - coceaero@mecanica.ufu.br

ATA DE DEFESA - GRADUAÇÃO

Curso de Graduação em:	ENGENHARIA AERONÁUTICA				
Defesa de:	PROJETO DE CONCLUSÃO DE CURSO - FEMEC43100				
Data:	06/04/2022	Hora de início:	08:00	Hora de encerramento:	09:38
Matrícula do Discente:	11621EAR002				
Nome do Discente:	PEDRO HENRIQUE BERNARDI FRANZINI				
Título do Trabalho:	Experimental analysis of the flow over an airfoil under ground and downforce effects .				

Reuniu-se remotamente, por meio da Plataforma Digital MS TEAMS, link de acesso https://teams.microsoft.com/l/meetup-join/19%3aR7f4giMtjZwwwXNR8mY4H_i7TWXJWAkpM_5dbpWs1K41%40thread.tacv2/1649107599834?context=%7b%22Tid%22%3a%22cd5e6d23-cb99-4189-88ab-1a9021a0c451%22%2c%22Oid%22%3a%227154176a-06de-4764-8a0d-65f93de5e3ac%22%7d, a Banca Examinadora designada pelo Colegiado do Curso de Graduação em Engenharia Aeronáutica, assim composta: Prof. Daniel Dall'Onder dos Santos, FEMEC/UFU; Giuliano Gardolinski Venson , FEMEC/UFU e Prof. Odenir de Almeida, FEMEC/UFU, orientador do candidato.

Iniciando os trabalhos, o(a) presidente da mesa, Prof. Odenir de Almeida, apresentou a Comissão Examinadora e o candidato, agradeceu a presença do público, e concedeu ao discente a palavra, para a exposição do seu trabalho. A duração da apresentação da discente e o tempo de arguição e resposta foram conforme as normas do curso.

A seguir o(a) senhor(a) presidente concedeu a palavra, pela ordem sucessivamente, aos(às) examinadores(as), que passaram a arguir o(a) candidato(a). Ultimada a arguição, que se desenvolveu dentro dos termos regimentais, a Banca, em sessão secreta, atribuiu o resultado final, considerando o(a) candidato(a):

Aprovado, Nota: 95.

Nada mais havendo a tratar foram encerrados os trabalhos. Foi lavrada a presente ata que após lida e achada conforme foi assinada pela Banca Examinadora.

Documento assinado eletronicamente por **Odenir de Almeida**, **Professor(a) do Magistério Superior**, em 06/04/2022, às 09:50, conforme horário oficial de Brasília, com fundamento no art. 6º, § 1º, do Decreto nº 8.539, de 8 de outubro de 2015.

Documento assinado eletronicamente por **Giuliano Gardolinski Venson**, **Professor(a) do Magistério Superior**, em 06/04/2022, às 09:50, conforme horário oficial de Brasília, com fundamento no art. 6º, § 1º, do Decreto nº 8.539, de 8 de outubro de 2015.

Documento assinado eletronicamente por **Daniel Dall'Onder dos Santos**, **Professor(a) do Magistério Superior**, em 06/04/2022, às 09:58, conforme horário oficial de Brasília, com fundamento no art. 6º, § 1º, do Decreto nº 8.539, de 8 de outubro de 2015.

A autenticidade deste documento pode ser conferida no site https://www.sei.ufu.br/sei/controlador_externo.php?acao=documento_conferir&id_orgao_acesso_externo=0, informando o código verificador **3499585** e o código CRC **0E9328EE**.

Referência: Processo nº 23117.023285/2022-69 SEI nº 3499585

À minha família, por sua capacidade de acreditar em mim, de me amar. À minha mãe, à minha irmã e ao meu falecido pai cujo sonho era me ver formado. Seus cuidados, apoios, conselhos e dedicação foram determinantes para eu seguir em frente. Pai, seja onde você estiver, sempre levarei seu legado no meu coração!

ACKNOWLEDGEMENTS

First of all, I would like to thank Prof. Dr. Odenir de Almeida for guiding me with dedication and proactivity in my course conclusion thesis. And also the technician Reinaldo Tomé Paulino, for the attention and help in the finalization of the test models and for the help in the manual fabrications.

I thank the course coordinator, Prof. Dr. Giuliano Gardolinski Venson, for his dedication to improving and maintaining the quality of the Aeronautical Engineering course at UFU.

I thank my mother, my sister and my late father for all the support, respect, patience and encouragement given throughout these years of college.

I thank all the friends I made on this journey (Giovanni, Vitor, Gabriel, the twins Vitor and Lucas, Raul, João, Paulo...) for being by my side, for helping me in the difficulties and for making this difficult path more appreciative.

”O Dado mais importante que separa o ser humano de todos os seus irmãos e primos da escala filogenética é o conhecimento; só o conhecimento liberta o homem, só através do conhecimento o homem é livre e em sendo livre: ele pode aspirar uma condição melhor de vida para ele e todos os seus semelhantes.”

(Prof. Dr. Enéas Ferreira Carneiro)

FRANZINI, P. H. B. **Experimental analysis of the flow around an airfoil under ground and downforce effects.** 2022. 86 p. Trabalho de Conclusão de Curso, Faculdade de Engenharia Mecânica, Universidade Federal de Uberlândia, Uberlândia.

ABSTRACT

All postulates in applied aerodynamics regarding the study of flow in airfoils have the primary purpose of discovering the relations of lift and drag forces. The main purpose of the present work is to study the relationship between the negative lift force (known as downforce) of an arched airfoil for racing car purposes; with its distance from the ground, characterizing the ground effect. The aerodynamic drag force under these same conditions is also evaluated. Furthermore, the aerodynamic behavior of the wing is evaluated under the same conditions with the presence and absence of plates installed at the tip of the wing, known as endplates, which would theoretically reduce the wingtip vortices of the airfoil. For this purpose, a small wind tunnel, an aerodynamic scale, a Pitot tube, and a physical assembly of the wing coupled to the measurement system are used; being, therefore, a mostly experimental work.

Keywords: Downforce. Ground Effect. Endplate. Airfoil. Cars aerodynamics

RESUMO

Todos os postulados em aerodinâmica aplicada no que concerne ao estudo do escoamento em aerofólios têm como finalidade primordial descobrir as relações de força de sustentação e arrasto. O presente trabalho tem como finalidade primacial o estudo da relação entre a força de sustentação negativa (conhecida como downforce) de um aerofólio arqueado para propósitos de carros de corrida; com a distância deste em relação ao solo, caracterizando o efeito solo. Também é avaliado a força de arrasto aerodinâmico nessas mesmas condições. Outrossim, é avaliado nas mesmas condições o comportamento aerodinâmico da asa com a presença e a ausência de placas instaladas na ponta dela, conhecidas como endplates, que teoricamente reduziriam os vórtices de ponta de asa do aerofólio. Utiliza-se para este fim um túnel de vento de pequeno porte, uma balança aerodinâmica, um tubo de Pitot, e uma montagem física da asa acoplada ao sistema de medição; sendo, portanto, um trabalho majoritariamente experimental.

Palavras-chave: Downforce. Efeito Solo. Endplate. Aerofólio. Aerodinâmica de veículos.

LIST OF FIGURES

LIST OF TABLES

LIST OF ABBREVIATIONS AND ACRONYMS

CAD	Computer Aided Design
CFD	Computational Fluid Dynamics
LAEX	Experimental Aerodynamics Laboratory

LIST OF SYMBOLS

C_L	Lift Coefficient of Wing
C_l	Lift Coefficient of 2D-Airfoil
C_D	Drag Coefficient of Wing
C_{D_i}	Induced Drag Coefficient
C_d	Drag Coefficient of 2D- Airfoil
C_M	Moment Coefficient of Wing
C_m	Moment Coefficient of 2D-Airfoil
ρ	Fluid density or specific mass
∇	Gradient of partial derivatives: $\nabla = \vec{i}\frac{\partial}{\partial x} + \vec{j}\frac{\partial}{\partial y} + \vec{k}\frac{\partial}{\partial z}$
t	Time
μ^{eff}	Effective Viscosity Coefficient
μ	Dynamic Viscosity Coefficient
ν	Cinematic Viscosity Coefficient
$\vec{v}$	Velocity in vector: $\vec{v} = u\vec{i} + v\vec{j} + w\vec{k}$
U_∞	Velocity of the flow (Modulus)
Re	Reynolds number
L	Length
c	Wing Chord
S	Wing Area
b	Wingspan
α	Angle of attack of the Wing
h	height
h/c	Dimensionless height

CONTENTS

1 INTRODUCTION

The postulates of aerodynamics emerged even before any documentation in mathematical language on the subject when they were empirically used in, for example, sailboats and windmills, whose physical phenomena are interrelated to aerodynamics, such as the concepts of pressure gradient and continuity of the air-fluid flow, all this already had their primitive explanations coming from the Greek philosophy.

Archimedes, Thales and Aristotle are registered as the first ones to carry out a study on aerodynamics in general, but still without a formal development of a scientific theory, which would only appear in the 17th century with Sir Isaac Newton, who developed the theory of air resistance. The evolution of the use of such postulates for aeronautics itself came with the Englishman Sir George Cayley, whose studies in applied fluid mechanics were a precursor to the discovery and definition of the four aerodynamic forces of flight: weight, lift, aerodynamic resistance and buoyancy, as well as the inter-dependence between them.

After such axioms had already reached a large part of engineering scientists, the Prussian-German Otto Lilienthal, in the 19th century, was the first to propose curved lines that could optimize the lift-drag ratio for higher values, which enabled the creation of surfaces defined by such curves with the aim of simply… flying. Such an invention was called the wing. The first data needed to define what exactly a wing consists of is its geometry, its typical shape. It was defined throughout history (and through experiments) that the wing would have an elongated shape transversely to the vehicle, with a curved cross section in a certain way to generate lift. A typical geometry of a wing is seen in figure 1.

Figure 1 – 3D drawing of a typical wing structure

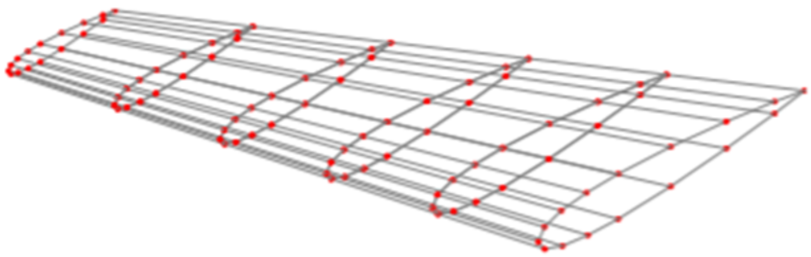

Source: Técnico Lisboa

After decades of improvement of knowledge in wings/airfoils to be applied in the development of the aeronautical industry, already in the 20th century, more precisely in the 1960s, the concepts of wings started to attract attention of engineers and designers of race cars. They saw the effect of lift in aeroplanes and, associating the similarities between the high speed of their cars with the need for them to make turns as quickly as possible as this kind of competition demands, they had the idea of reversing the wing (literally putting an aeroplane's airfoil upside down) and producing an negative lift and attaching such a wing to the car with the primary objective of increasing the normal force between the car's wheels and the ground, causing the grip between the tire rubber and the ground to increase massively and consequently increasing the car's speed and control in curves. The negative lift had started to be called as downforce. The first car to have a wing attached to it was the Formula One car Lotus 49 (Figure 2), designed by the engineer legend Colin Chapham (Figure 3). This evolution is cited by Katz about the race cars wings (KATZ, 2006):

> Airplane wing design matured by the middle of the twentieth century and it was only natural that race car designers borrowed successful airplane wing profiles to use on their vehicles. However, this approach was not entirely successful due to the inherent differences between these two applications. The difficulties in this technology transfer were highlighted by Katz (1994) and his findings can be summarized as follows: A race car lifting surface design is different from a typical airplane wing design because (a) a race car's front wings operate within strong ground effect, (b) open-wheel race car rear wings have very small aspect ratio, and (c) there are strong interactions between the wings and other vehicle components (e.g., body, wheels, or other wings).

Figure 2 – The Lotus 49 car in the 1969 Monaco Grand Prix

Source: Classic Team Lotus

When the British driver Graham Hill won that race, and would eventually win the 1968 championship, soon every team in Formula One started to attach wings to their cars and then it became a standard on the sport since today, and establishing itself as perhaps the most crucial component to car performance, so, of course, all the formula one teams started to develop upgrades in the wing technology.

Figure 3 – Colin Chapman himself

Source: Wikipedia

Almost ten years later, years of development of the cars wings, the Formula One reached a new level of creating downforce. In 1977, with the so named Lotus Type 78, was the Formula One car that pioneered the application of the ground effect. Again with Colin Chapman, the still head of the Lotus team, he performed routine reviews of certain areas of the team when deciding to return to principles basic design. While his engineers were working on their prototype sidepods, Chapham came up with the idea of making them in an airfoil shape and testing them in the wind tunnel. The results were surprising: the car's downforce had increased a lot without having a big increase in drag. The team even experimented this with a car with ground effect in 1977, but it was the following year that the technology was finally implemented. The team won eight races that year and won the constructors' world championship and the drivers' world championship with Mario Andretti.

The key to the success of this concept was to explore an aerodynamic principle called the Venturi effect, whereby the underside of the car could be designed so that it would act as a large wing (Figure 4), which would suck the car into the ground. The Lotus 78 gave an indication of what could be gained from the low-pressure environment created by the side skirts; however, it was the Lotus 79 that refined this concept and capitalized on the advantages of Venturi diffusers and tunnels (PIOLA; SOMERFIELD, 2020).

Figure 4 – Lotus 79 design showing the airfoil profile on the car floor in yellow

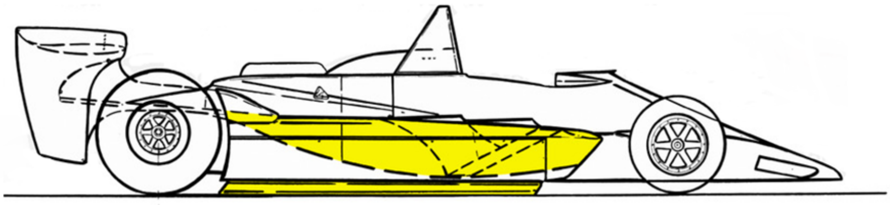

Source: https://motorsport.uol.com.br/f1/news/analise-tecnica-lotus-79-como-um-erro-ajudou-a-criar-um-icone-da-f1/4795093/

Although the ground effect is really very strong in creating downforce with as little turbulence as possible, the technique of making an airfoil on the floor of the car was banned from Formula 1 in 1983 because the knowledge of this subject at the time meant that the generated downforce had great variations with the airflow, and when one car was positioned behind another, it would vary that airflow greatly and cause the control of the car behind to become unpredictable. This ended up causing many serious accidents, including some that were fatal, such as the accident of Canadian driver Gilles Villeneuve at the 1982 Belgian GP. In this way, the category preferred that the cars become slower, but safer and more predictable from 1983 onwards. However, Formula 1 is returning with the use of ground effect from the 2022 season, believing that nowadays it is already possible to control the unpredictability of the airflow; and they are doing this with the objective of reducing the turbulence generated by the wings and favoring the overtaking maneuvers. Figure 5 demonstrates the evolution of Formula 1 cars throughout its 72 years of existence, with the addition of both front and rear wings, with a much more complex geometry.

From then on, downforce-focused airfoils continued to be developed and used both in single-seater categories, such as Formula 1 itself or Indycar, and in sports street cars, such as Bugatti (figure 6), Ferrari, Porche, Mercedes, Lamborghini, and others.

Figure 5 – The prototype of the 2022 car presented by the FIA at the 2021 British GP

Source: https://www.formula1.com/en/latest/tags.2022-car.6glC1hbbpRSV27ssTflMg1.html

Figure 6 – Bugatti Veyron with airfoil

Source: Wikipedia

Another, simpler innovation for racing cars was the so-called endplates, which consist of plates placed on both ends of the wing. Its function, basically, is to increase the ratio between lift and drag, improving the efficiency of the wing. You can see an example of the endplate on the front wing ends of the formula 1 car in the figure 5. The more physical details of how endplates help the aerodynamic performance of wings are explored in the theoretical foundation and literature review sections.

1.1 Motivations

From the last century to the present day, from George Cayley's prototype to today's very modern aircraft such as the Boeing 787; establishing a relationship of optimization of parameters so necessary that they ended up becoming postulates for the aerodynamic design of an aircraft. Such truisms can be cited: maximization of the relation between lift and drag coefficients, interaction of airflow with solid surroundings (both of the aircraft itself, and of the environment itself), structuring and fixing of airfoils, among others.

As for automotive aerodynamics, basically all concepts arising from the aeronautical industry in this subject can be extrapolated and adapted for motorsport: a rear wing with an optimized C_L/C_D ratio to produce downforce will keep the vehicle with more grip on the ground, improving its rear stability and its performance in curves, allowing the car the possibility of being able to turn faster and with more precise, more stable and more predictable steering compared to the vehicle without the presence of the wing (the latter also improves the safety of the wing), especially if it is a competition car, as handling the aerodynamic adjustment can prevent the loss of rear control during corners - the so-called oversteer (FARON *et al.*, 2015).

There are, therefore, major challenges in terms of aerodynamics for the design of a prototype of an airfoil to evaluate the ground effect (present in racing cars), such as:

- The relationship between the length of the airfoil string (c) and its height above the ground; (h);
- The effects of inserting and removing endplates;
- The way the airfoil is attached to the car, which needs to interfere with the airflow as little as possible in order not to produce an unwanted drag force;
- The airfoil manufacturing process, as it has a complex geometry;
- The effects of roughness on the surface of the airfoil, which, according to the theory of fluid mechanics, must have the lowest possible roughness in order to have high efficiency of the aerodynamic properties of the airfoil.

The objective is, therefore, to evaluate parameters such as pressure distribution, downforce distribution and drag for a high curvature airfoil whose geometry is ideal for high lift production at low speeds. Having such an airfoil designed by CAD, the idea is to physically build it and couple it to a balance of aerodynamic forces and test the behavior of such forces with the angle of attack and ground clearance as variable parameters. In this way the results will quantitatively show the consequences of the ground effect for this specific type of airfoil.

2 THEORETICAL FOUNDATIONS

2.1 Fundamental equations

Any compressibility effect of the flow is negligible, then shall be dis-considered for the present work. Any heat exchange will also be neglected, dispensing with any concern with the energy equation. This happens because there are only two variables that have more relevant variation: pressure and velocity. Thus, they are governed by only two basic concepts of fluid mechanics, the conservation of mass and Newton's second law. Each of them is represented mathematically through a partial differential equation, according to the concepts of differential and integral calculus, present in the concepts of fluids' mechanic (TANNEHILL *et al.*, 1984).

$$\frac{d\rho}{dt} + \nabla \cdot (\rho \vec{v}) = 0 \tag{2.1}$$

The equation of conservation of mass (2.1) presented is in differential form and imposes that the mass in a given volume varies in time only as a function of the scalar and vector fields density (ρ) and velocity ($\vec{v}$) respectively. In this way, it is proved that there is no creation of matter (and therefore of mass). However, in flows with two or more phases, the equation could present a different way to deal with phase transformations, which would cause variations in the amount of each phase not only due to fluid movement; however, this will not be the case for the present work.

The second fundamental equation is the momentum conservation equation (2.2) that is related to the foundations of Newton's second law.

$$\frac{\partial(\rho \vec{v})}{\partial t} + \nabla \cdot (\rho \vec{v}\vec{v}) = -\nabla p + \nabla \cdot (\mu^{eff} \nabla \vec{v}) + \vec{S}_M \tag{2.2}$$

The transient term in the momentum conservation equation represents the accumulation of momentum through time, and the second term describes advection momentum flux. The first two terms on the right side of the momentum conservation equation represent momentum imparted due to pressure and viscosity, respectively, while the third term in this part from the right corresponds to the linear momentum source.

Finally, there is the Bernoulli equation, which consists of a simplification of the analysis of two different phases of a flow considering their respective energies. It is obtained by integrating Euler's equations, or by applying the law of conservation of energy in two sections along the stream, and neglecting effects such as viscosity, compressibility and thermal effects. Such an equation may not be very precise, but its simplicity is ideal for qualitatively evaluating the behavior of certain flows.

For v being the modulus of the velocity of a given fluid, ρ its density, g for the gravity acceleration, h its height in relation to a given reference point, the Bernoulli equation (2.3) develops according to two different phases (1 and 2) of the flow.

$$\frac{1}{2}\rho_1 v_1 + \rho_1 g h_1 + P_1 = \frac{1}{2}\rho_2 v_2 + \rho_2 g h_2 + P_2 \tag{2.3}$$

The three summation terms for the two sides of the equation refer to the fundamental form of energy in a flow: kinetic energy, gravitational potential energy, and pressure energy.

2.2 Reynolds Number

Uttered and defined by Osborne Reynolds in 1883, the Reynolds number (*Re*) is a dimensionless number used in fluid mechanics, hydrodynamics and aerodynamics in general to calculate the flow regime - determining such a regime as laminar, turbulent or transient - of a certain fluid. The Reynolds number in practice consists of a ratio of inertia forces to viscous forces, which is defined by the equation number 2.4.

$$Re = \frac{\rho U_\infty L}{\mu} = \frac{U_\infty L}{\nu} \tag{2.4}$$

The length L is the easiest to confuse as it consists of a characteristic and arbitrated length. For pipes, it is considered its diameter, for an airfoil, it is considered to be its chord (c).

The Reynolds number thus quantifies the fluid flow behavior, which can be divided into three regime classifications (Figure 7).

Laminar flow occurs when the particles of a fluid move along well-defined paths, presenting sheets or layers (hence the name laminar), which preserve their characteristics during flow.

Turbulent flow occurs when the particles of a fluid do not move along well-defined paths, that is, the particles describe irregular trajectories, with random motion, producing a transfer of momentum between regions of liquid mass. This flow happens mostly in high Reynolds number.

Transient flow, on the other hand, is more difficult to predict in nature as it combines characteristics of both laminar and turbulent flow without having the possibility to determine a percentage trend.

Figure 7 – Fluid streamlines playfully demonstrating the three types of flow: laminar, transient and turbulent

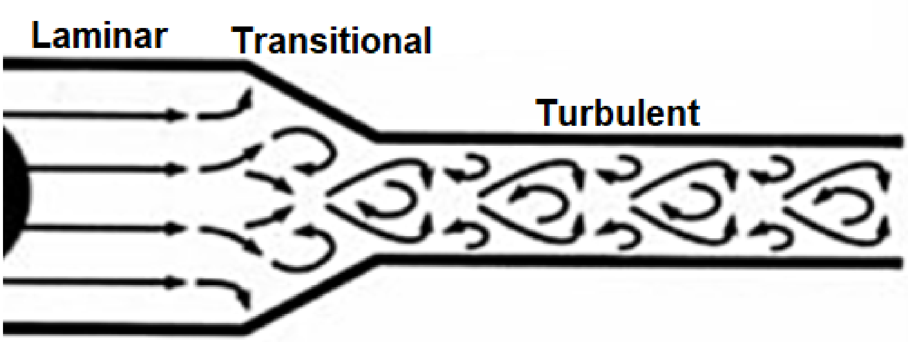

Source: https://www.guiadaengenharia.com/

Low Reynolds number flows, as the experiment will have a reynolds number in the order of magnitude of 10^5, considered aerodynamic low, are characterized by increased influence of the viscous forces of the fluid compared to inertial forces (WINSLOW J.; OTSUKA, 2017). According to such literature, this characteristic of the low Reynolds number had the consequences: laminar-turbulent transition phenomena, laminar separation bubbles and reattachment of the boundary layer, whose details are explained in the Boundary Layer section.

2.3 Aerodynamic concepts

2.3.1 Aerodynamic coefficients: lift and drag

The lift coefficient, C_L, is basically the relationship between the lift pressure and the dynamic pressure, and the pressure on the bottom (the bottom torso) of a given geometry must be greater than the pressure on the upper torso for there to be a positive lift and vice versa for that there is a negative lift (downforce). In wings, lift is a function of the shape of the wing airfoil and the angle of attack (α), which is the angle at which the airfoil is in relation to the airflow; each angle of attack produces a particular coefficient of lift, since the angle of attack is the controlling factor in the distribution of pressure on an airfoil (ANDERSON, 2001). In a simplified way, it is the ability that has a certain profile to generate lift.

For a given geometry, it is possible to define coefficients from which the forces and moment acting on it can be calculated as a function of the pressure dynamics, q_∞, and a reference area, A, and the lift force itself L. The dynamic pressure is calculated by Equation 2.5.

$$q_\infty = \frac{\rho U_\infty^2}{2} \tag{2.5}$$

The lift coefficient, C_L, itself, is calculated by:

$$C_L = \frac{L}{q_\infty A} \tag{2.6}$$

The drag coefficient, or aerodynamic drag coefficient, C_D, is, like the lift coefficient, a dimensionless number that quantifies the drag force or drag of an object in a fluid medium taking into account purely its geometry. The drag force (D) can be defined as the expansion of the drag coefficient (C_D) taking into account the dynamic pressure of the medium (q_∞) and the reference area (A) - similarly to C_L.

$$C_D = \frac{D}{q_\infty A} \tag{2.7}$$

Drag is divided into two types:

- Parasitic drag, which appears in the geometry of the body submerged in a fluid flow, regardless of whether the body is producing lift. The higher the flow velocity, the greater the parasitic drag.
- Induced drag, which appears as an inevitable component of lift, that is, it results from the difference in pressure between the bottom and the upper torso of the airfoil, which proves that the greater the lift, the greater the induced drag. At lower speeds, the induced drag tends to be greater than at higher speeds since in this slower condition, the airfoil needs a greater angle of attack in order to produce efficient lift; and the greater the angle of attack, the greater the longitudinal component of force towards the trailing edge of the wing, that is, the greater is the induced drag.

As already specified in the present work in the motivation section, the main goal in general of an efficient airfoil is to maximize the $\frac{C_L}{C_D}$ ratio, that is, the highest possible lift with the least drag possible is desired.

However, it is not possible to deduce a direct mathematical relationship between the lift coefficient and the airfoil geometry, as this geometry is always very complex and difficult to define. Regarding the angle of attack, there is a region in which there is a direct proportion between the angle of attack itself and the lift coefficient (Figure 8), the higher the α, the higher the lift coefficient. In the case of an airfoil that produces downforce, the same principle applies, but with C_L increasing its modulus, however, negatively, making the ratio between C_L and C_D modular $\left(\left|\frac{C_L}{C_D}\right|\right)$ so as not to compromise the analysis to maximize this term.

Figure 8 – Typical C_L x α curve of an airfoil

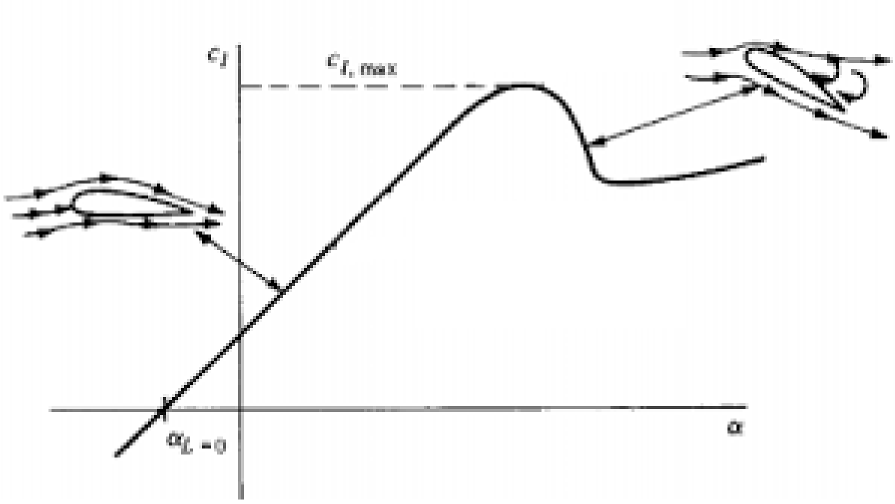

Source: (TANNEHILL *et al.*, 1984)

The region of direct proportion between alpha and C_l is, however, limited by the so-called stall angle (the angle which occurs the $C_{l,max}$), which abruptly reduces lift and makes the aircraft enter the infamous stall. The physical nature of the stall can be explained by the **Boundary Layer** concept.

2.3.2 Boundary Layer

In the year of 1904, Ludwing Prandtl proved that, for an sufficiently high Reynolds numbers, in a region of the flow close to an aerodynamic surface the flow will depend heavily on viscous effects, while outside it it could be described satisfactorily without regard to viscosity. In other words, when any body is submerged in a flow of velocity U_∞, the regions very close to it will have a velocity lower than U_∞ until it is zero when the fluid particle adheres to the surface of the body.

There are some types of boundary layer: of velocity, of temperature, of concentration... The two first are the most common in studies and are shown in Figure 9.

Note from the figure that the velocity boundary layer thickness (δ) is defined for when the velocity at this boundary exceeds 99% of U_∞; and below it, towards the body, the flow velocity is reduced to zero thanks to the viscosity of the fluid, which is shown in the velocity

Figure 9 – Theorical Representation of thermal and velocity boundary layers on a flat board

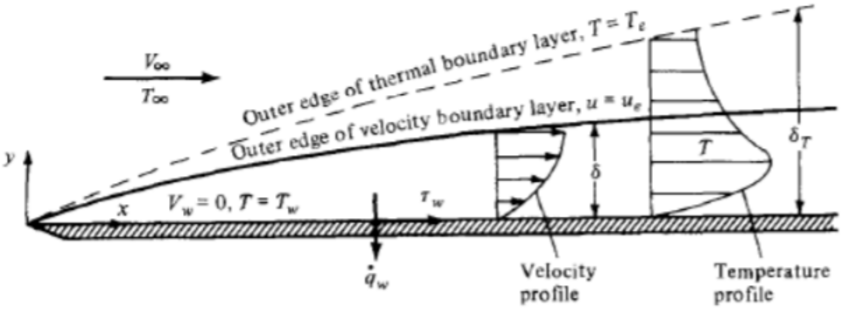

Source: Anderson (2001)

profile graphic.

Other definitions used consider fluid displacement produced by the boundary layer, or the equivalent loss of linear momentum. There are divisions within the boundary layer itself. In the region closest to the wall, a laminar sublayer, dominated by viscous effects. On the outermost, a sublayer where turbulent effects predominate. There would be an intermediary between these two, which would be a transition region, whose concepts are directly interconnected with the magnitude of the reynolds number, and the fluid behavior also behaves similarly to the Figure 7.

When pressure forces are greater than inertia forces, the flow changes direction. This tends to happen as the flow travels through the body, which causes the energy of the flow to decrease thanks to the weakening of viscous forces and, consequently, the pressure gradient $(\frac{dp}{dx})$ becomes bigger than zero... In this way, the variation of velocity in relation to the vertical dimension along the body $(\frac{\partial u}{\partial y})$ is changed (see Figure 10). At this point, the detachment of the boundary layer is visible and the infamous stall happens.

The Figure 10 shows the physics of the effect described: the flow velocity in the regions closest to the body is reduced thanks to the adverse pressure gradient, reaching a moment when such velocities reverse direction in these regions, generating eddies. This is the practical visualization of boundary layer detachment, which in general terms should be avoided as much as possible or at least delayed as much as possible, since the interaction between the body and the fluid particles in the boundary layer is a requirement to produce the force of aerodynamic lift. In addition, with detachment, the existence of vortices causes a large increase in the drag force. Thus, in summary, detachment reduces C_L and increases C_D, and is therefore very harmful to maintain the desirable $\left|\frac{C_L}{C_D}\right|$ ratio.

The general behavior of the boundary layer, such as the flow regime or the nature of the detachment, are primarily determined by the geometry of the body that is submerged in the

Figure 10 – Velocity field ($u(x)$) inside the boundary layer of any body with the B.L. detachment

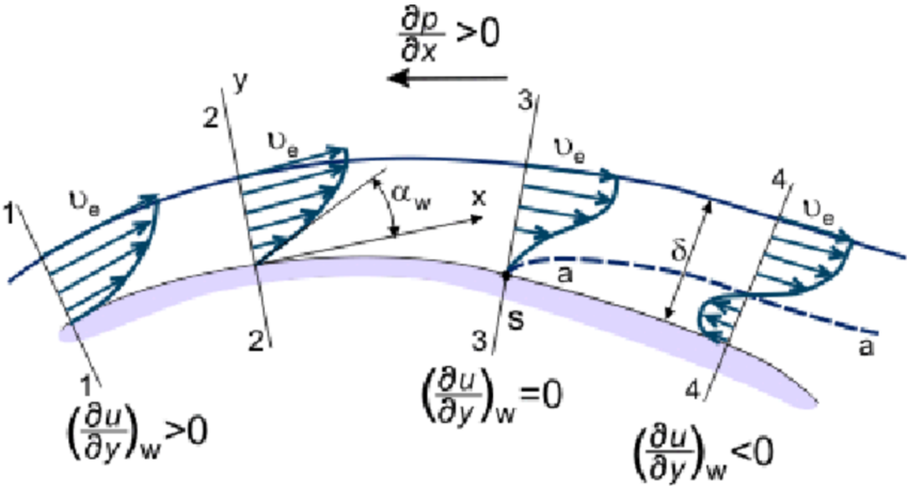

Source: <https://www.researchgate.net/figure/Boundary-layer-and-flow-separation_fig7_291821947>

flow, and from this comes the typical characteristic of airfoils (see Figure 1): rounded bodies, with edges more aggressive leading edges than the trailing edges, which have a smoother decay in order to avoid the detachment of the boundary layer.

2.4 Ground Effect

When the lift force exists, a wing creates large rotating air masses at its tips. Such support occurs due to a lower pressure on its upper surface in relation to the bottom surface. This pressure difference generates lift as already said but, at the same time, there is an inevitable flow of air that hinders the flight as the high pressure flow from the underside of the wing tries to circulate to the low pressure area at the top of the wing, at the tips of the wings. This movement is called a **vortex**.

Figure 11 – Front view of a generic wing, highlighting the air direction at the wing tips (vortex)

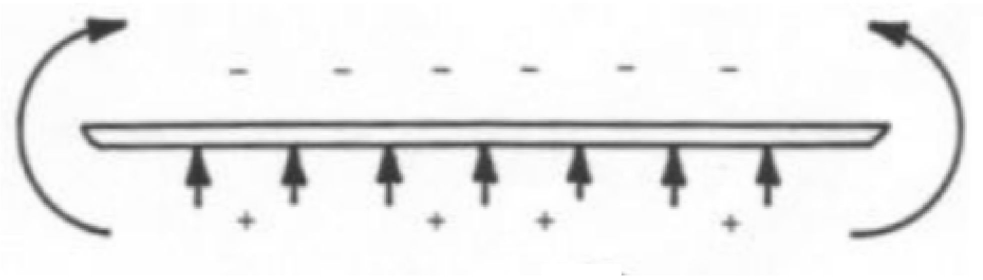

Source: http://www.espiral.com.pt/docs/EfeitoSolo.pdf

As the aircraft or the winged vehicle travels forward, they cause the vortex constantly, leaving a vortex trail generated by each of the two wingtips - while at one of the wingtips, the vortex rotates in one direction, at the other, it rotates in the opposite direction as shown in Figure 11. In general, this vortex are undesirable, as this disturbs the laminarity of the airflow, creating velocity outside the direction of the flow since, mathematically, the quantification of the vortex, the vorticity ω, consists of the vector field defined by the curl of the motion field (the vector velocity $\vec{v}$) as shown in the equation 2.8.

$$\omega = \nabla \times \vec{v} \tag{2.8}$$

Analyzing the vorticity, it is possible to conclude that the ideal to reduce it would be to change the flow direction, reducing the vector modulus to calculate the gradient in the vector product, in other words, the vortex should change its linear. A universally adopted solution for aircraft was the construction of a physical barrier at the wingtip in order to cause this change in the flow direction and consequently reducing the wingtip vortex. Such a solution were the **winglets**, as shown in the Figure. For a vehicle with an airfoil, the same principle applies, with the so-called **endplates**.

Figure 12 – Both anti-vortex models installed on the tip of a wing

(a) Model of a typical winglet

(b) Model of a typical endplate used in sport cars

Source: 3D Warehouse - SketchUp

In a more pragmatic way of saying, aircrafts in general achieve a greater lift force for the same angle of attack (although with a reduction in the maximum lift force), also better efficiency flying close to the ground and are mainly affected in the takeoff and landing processes - in this one, the ground effect is undesirable. This effect is caused by a cushion of compressed air between the wings and the ground. However, tests in wind tunnels indicated that while this effect is present, the ground effect is almost solely due to the interruption of the formation of the wingtip vortices, which reduces the induced drag. These vortices destroy a large amount of the lift generated by the wing through the loss of induced drag, and by eliminating them it increases the wing's efficiency. Namely, the increase in lift created by the Ground Effect comes primarily from a reduction in the amount of the induced drag generated which improves the $\left|\frac{C_L}{C_D}\right|$ ratio.

Trivially, the reduction in induced drag is proportional to the height of the wing above the ground. The Figure 13 demonstrates the dimensionless height - in percent - between the total induced drag of the wing at a certain angle of attack in relation to the height of the ground; Note that the ground effect ends approximately when the height of the ground equals the wingspan. It is worth remembering that it consists only of a general rule and particularities of airfoils can reasonably change the behavior of induced drag; detailed aspects of a specific airfoil will be considered in subsequent studies in this report, thus this can't be considered as a rule.

Figure 13 – Generic analysis of the percentage of induced drag for an aeroplane as a function of height to the ground in percentage of wingspan.

Source: https://skybrary.aero/articles/ground-effect

In ground effect, the angle of attack required before a wing stalls, for a given amount of lift, is reduced. The extent of this decrease in stalling angle of attack will vary according to the nature of the airfoil, but can be several degrees. The difference will also be affected by any reduction in the maximum lift coefficient of a particular wing in ground effect, compared to that coefficient in free air (SKYBRARY, 2012).

Just as practically all theoretical concepts about aircraft wings are extrapolated to

Figure 14 – Difference between the lift behavior of an aircraft wing with and without ground effect

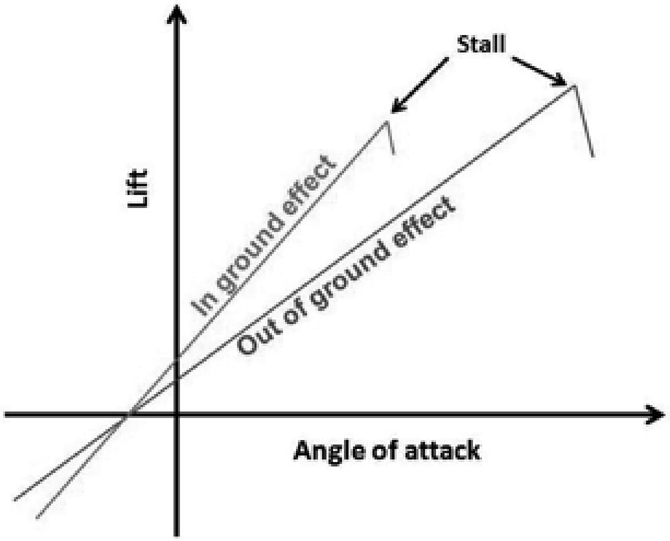

Source: (SKYBRARY, 2012)

car wings (downforce wings), the concepts of ground effect can also be extrapolated and an introduction on this subject has already been made in the introductory section of this work.

Under ground effect, the flow dynamics tends to be, in a way, optimized, as the breaking of the vortices thanks to the physical presence of the "ground" makes the vortices, which cause drag (Figure 11), not complete. And the downward direction of these vortices is blocked by the ground, causing a kind of "air pocket" just below the wing, optimizing the lift in general. Thus, in ground effect, the wing with less induced drag (less C_{D_i}) and also greater lift (higher $|C_L|$) is expected for both aircraft and downforce airfoils (for sports cars). The study of the behavior of a downforce airfoil, thus, follows the same theoretical foundations already presented, and is detailed and explored in the next section of bibliographic references.

3 LITERATURE REVIEW

Probably the first requirement to think about any endorsement of an airflow through a downforce airfoil under the ground effect is to understand the all postulates in vehicle aerodynamics: from topics such as the aerodynamic shape of the vehicle to the consequences of introducing a front or rear airfoil - ranging from the evaluation of flow to the consequences of loads on the vehicle, which aims to add stability and avoid understeer and/or oversteer. These references can be found by reading the premiere work of modern aerodynamics of vehicles (HUCHO, 1998).

Then, since the work is purely experimental, without any Computational Fluid Dynamics (CFD) assistance, assimilating the test in a low-speed wind tunnel (BARLOW *et al.*, 1999), which will be one of the most important objects of this project, is essential for comparison measures and analysis of several parameters related to the use of a wind tunnel. One of them is the design constraint for a low Reynolds number, which will also be applied in the present work. There is also the definition of low Reynolds number for this work, which is in the same region as the definition of external flows: in the order of magnitude of 10^5. Not only that, the equipment reported in the literature will give an idea of the accuracy and veracity of the results, as well as the possible variations that may occur due to the difference in equipment and analysis method; all in all, the literature includes:

- Important Parameters for Similarity;
- Types of Wind Tunnels and its consequences;
- Pressure, Flow, and Shear Stress Measurements;
- Forces and Moments from Balance Measurements;
- Flow visualization and others.

Details on the influence of laboratory components such as the wind tunnel and the balance of aerodynamic forces are covered in the Methodology section.

Already in terms of the experimentation itself, the first aerodynamic study of a wing in ground effect with a low surface near-ground pressure was performed in 1921 (ZAHM A. F.; BEAR, 1921) when the authors were investigating the effects of proximity to other bodies on the wing of an aircraft - without thinking about downforce. The data were lifted in a manner contrary to the sense of ground effect: with the ground “above” the aircraft wing, not below it. Their results were basically the first to demonstrate the ground effect, as the authors report precisely the large increases in lift force for several incidences and proximity to the ground.

Similarly, but now focusing on downforce, there was a study on the distribution of pressure field and forces resulting in a single element wing in a wind tunnel with rotating belt for various angles of attack and ground clearances (KNOWLES K.; DONOGHUE, 1994). An attempt was made to establish a mathematical relationship (and not purely experimental) between the ground clearance and the efficiency of the wing element, however, the limitations of the geometry made this impossible in that study. Even with this eventual "failure" in the elaboration of a result, the study brought the initiative to evaluate the lift coefficient, C_L, in relation to the height of the ground. However, as the characteristic of the airfoil is variable and can have different sizes, but proportionally similar, the dimensionless height, h/c, which takes into account the ratio between the height and the chord of the airfoil, was used in this study and the subsequent ones.

Probably the most important author for the motivation of this work is Joseph Katz (KATZ, 2006). His bibliography, like Knowles', empirically evaluates the internal and external agents that improve the vehicle's aerodynamic efficiency. The downforce reduction effect evaluated in the literature is a characteristic of the $C_L \times h/c$ curve in which the proximity to the ground initially increases the lift coefficient. But for regions very close to the ground, reaches a maximum and reduces the C_L again, performing inviscid simulations by using the method of panels on inverted wings of racing cars. He observed an asymptotic increase of the lift coefficient, without reduction, however, he comments and proves that, for regions really close to the ground, downforce would be limited by viscous effects. This even goes against the intuition of the theoretical foundation, where downforce should simply increase indefinitely as ground clearance decreases. This causes a peak of the lift coefficient, that is, a maximum value of C_L for an optimized dimensionless height. This experiment contradicts what was presented in the theoretical foundation (Figure 13), in which a direct and continuous relationship is established between the induced drag and the distance to the ground in a purely intuitive and theoretical way. However, and getting into one of the objectives of this work, which is the differentiation of the ground effect in wings producing lift in relation to wings producing downforce, both close to the ground; it was noted that the C_D of a wing producing downforce under ground effect is greater as the wing approaches the ground (Figure 15); unlike an aircraft wing, whose drag is lower the lower the h/c ratio. The explanation for this is that the significant increases in downforce (which consequently increases upwash, not downwash on aircraft wings) generate increasing induced drag and, for the downforce loss region, continued drag growth is caused by boundary layer separation (ZERIHAN; ZHANG, 2000). Since Katz demonstrated that lift does not work that way, his book therefore also evaluates the veracity of the graph shown in Figure 15 that the author took and analyzed from the literature (ZERIHAN; ZHANG, 2000). The graph places the tested airfoil at an angle of attack $\alpha = -1^{\circ}$, with a calculated Reynolds number of $Re = 2 \times 10^6$.

Figure 15 – $-C_L$ and C_D versus ground clearance $\left(\frac{h}{c}\right)$ for an inverted LS(1)-0413 airfoil

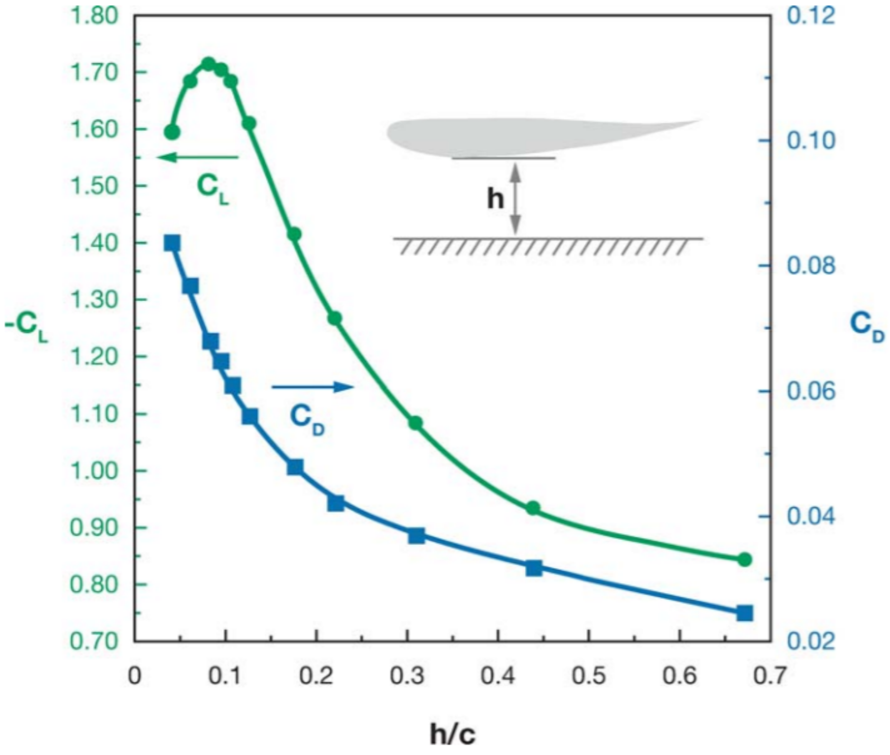

Source: (KATZ, 2006)

Zhang (ZERIHAN; ZHANG, 2000) points out that the phenomenon of downforce reduction to very low h/c is due to the combination of the gradual separation effects of the layer limit due to the high gradient in pressure recovery generated by the effect venturi (Dominy, 1992) and the slight reduction in pressure in the pressure surface.

As for the doctoral thesis by the same author (ZERIHAN, 2001), there were a series of evaluations both experimental and CFD, in which the flow behavior in the suction regions of a 3D wing producing downforce was analyzed, for three different dimensionless heights: $h/c = 0.134$, $h/c = 0.09$, $h/c = 0.067$. The Figure 16 demonstrates a visualization in oil in these regions and it is noted that for the lowest height, the oil mark is stronger and notably was subjected to a greater suction force while this effect is less visible for the oil mark in the highest height. Despite this big difference, in a practical way, the height difference between the three marks is too low, which proves the sensitivity of aerodynamic science especially on the ground effect.

Figure 16 – Oil flow visualization on suction surface, leading edge lowermost (a) $h/c = 0.134$ (b) $h/c = 0.090$ (c) $h/c = 0.067$

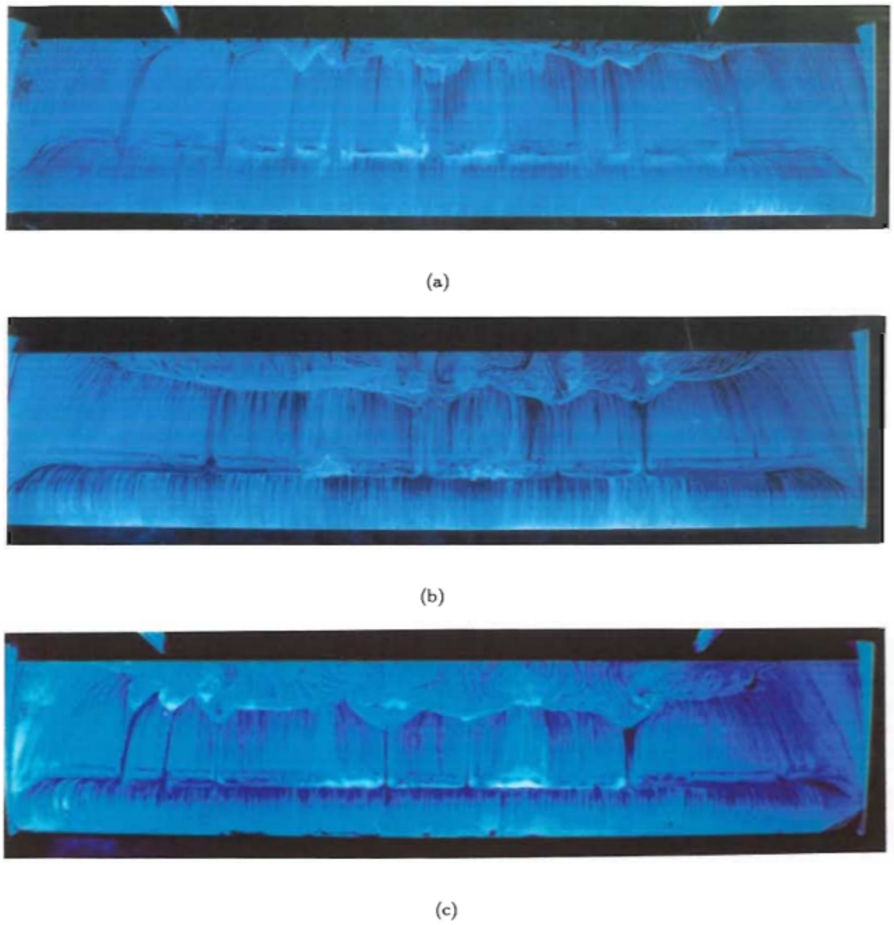

(a)

(b)

(c)

Source: (ZERIHAN, 2001)

Another important feature to note is the increase in the growth rate of C_L with proximity to the ground through the evolution of this pressure effect on the outer regions of the wing. This effect is attributed to the suction induced by the vortex generated at the edge of the endplate, known as the edge vortex. Due to the pressure difference between the sides of the endplate, there is infiltration of airflow from the outer endplate region to the lower low pressure inner region the wing (TOET W.; ZERIHAN, 2006). The interaction of this flow with the sharp edge of the plate generates a region of high shear due to separation. Similar to the delta wing lift mechanism of jet aircraft, the winding of the shear-separated layer becomes propagates forming a vortex inside the endplate which then flows downstream. This vortex is intensified in the region of increased downforce and disintegrates (vortex breakdown) in the region of slope reduction of the curve, as shown in Figure 17. The eventual reduction in downforce is due to the wing stall.

The dimensionless distance to the ground also affects the $C_L \times \alpha$ curves of the airfoil, since the increase in the angle of attack completely changes the behavior of the coefficients

Figure 17 – Separation in the C_L curve (a) and the edge vortex influence detailed (b)

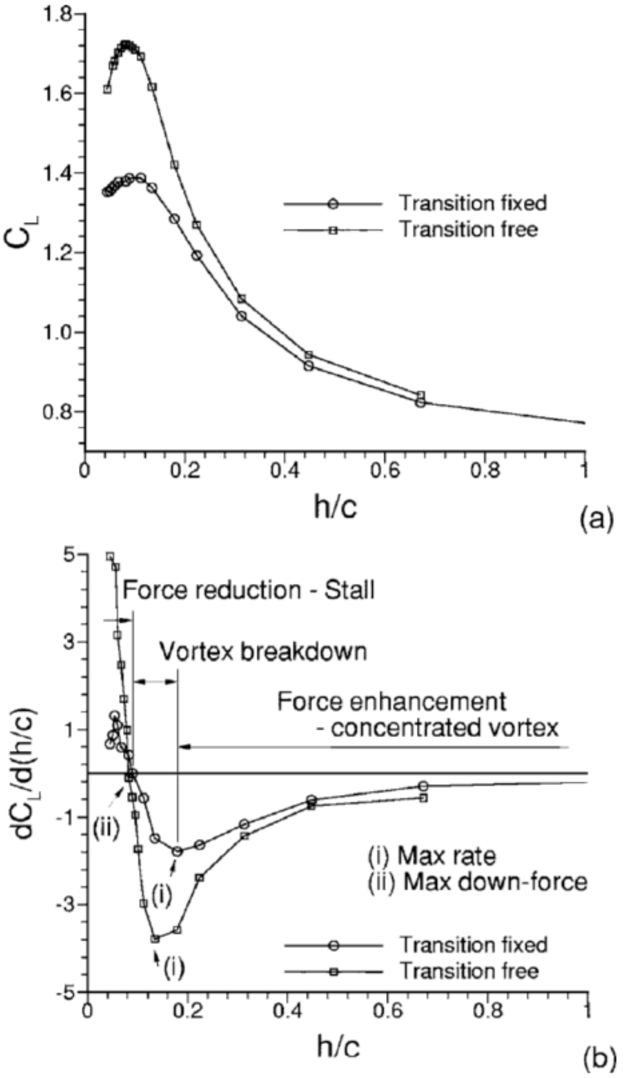

Source: (TOET W.; ZERIHAN, 2006)

C_L and C_D and they depend heavily on Re on a free flow (E423...,). The study (ZERIHAN; ZHANG, 2000) shows in Figure 18 that the higher the α, the lower the wing's response to the physical impositions caused by the ground effect, one of which is the continuation of the increase in maximum downforce. The combined effect of generating greater pressure gradients on the wing due to increased incidence α and proximity to the ground result in detachments occurring earlier at higher angles of attack.

One of the main starting points of this thesis comes from a patent with a self-explanatory name: "Wing in ground effect vehicle with endplates" (ALLEN, 2001). This demonstrates, particularly in the table present in the Figure 19. The patent reports on the addition of different endplates and their effects on the edge vortex that, as already reported in the theoretical foundation section, the abrupt change in the direction of the wing geometry at its

Figure 18 – $C_L \times \alpha$ curve with different h/c for an determinate airfoil

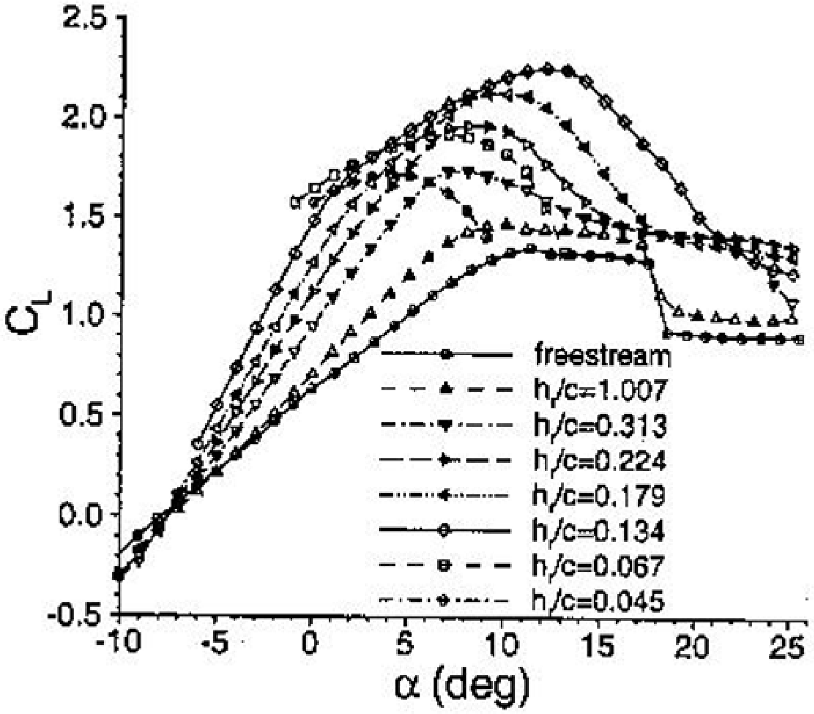

Source: (ZERIHAN; ZHANG, 2000)

tip causes a great change in the vorticity equation 2.8 as it is a cross product whose three unit vectors ($\vec{i}$, $\vec{j}$ and $\vec{k}$) have equal weight in the definition of the vortex tensor.

Figure 19 – Comparison of the behavior of a wing with two types of endplates: flat and deep, and curved and shallow

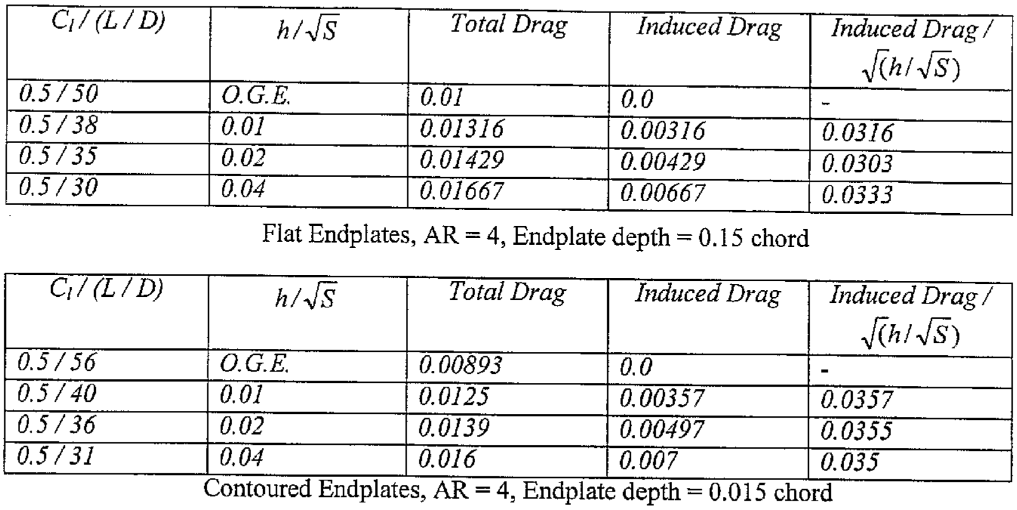

C_l / (L / D)	$h/\sqrt{S}$	Total Drag	Induced Drag	Induced Drag / $\sqrt{(h/\sqrt{S})}$
0.5 / 50	O.G.E.	0.01	0.0	-
0.5 / 38	0.01	0.01316	0.00316	0.0316
0.5 / 35	0.02	0.01429	0.00429	0.0303
0.5 / 30	0.04	0.01667	0.00667	0.0333

Flat Endplates, AR = 4, Endplate depth = 0.15 chord

C_l / (L / D)	$h/\sqrt{S}$	Total Drag	Induced Drag	Induced Drag / $\sqrt{(h/\sqrt{S})}$
0.5 / 56	O.G.E.	0.00893	0.0	-
0.5 / 40	0.01	0.0125	0.00357	0.0357
0.5 / 36	0.02	0.0139	0.00497	0.0355
0.5 / 31	0.04	0.016	0.007	0.035

Contoured Endplates, AR = 4, Endplate depth = 0.015 chord

Source: (ALLEN, 2001) - Adapted

It can be seen from the table that the lift coefficient is higher for OGE regions, and reduces as the dimensionless distance increases (represented differently, by $h/\sqrt{S}$ rather than h/c), but for the flat endplate, the ratio between C_L and L/D, which according to the thesis evaluates in double multiplicity the geometric characterization of the endplate to produce negative lift is smaller for all heights in relation to the contoured endplates. A slight increase in C_D and C_{D_i} is also observed in the same situation.

4 METHODOLOGY

As already mentioned, the primary objective of the experiment is to evaluate a low Reynolds flow over and under a downforce airfoil varying 3 main parameters:

- The angle of attack α of the airfoil;
- The height h of the airfoil above the ground;
- The presence (or not) of endplates.

For each different height h, which starts very close to the ground, the angle of attack α of 0°, 4°, 8°, 12° and 14° will be varied in order to obtain the lift and drag modulus of force and, with the equations 2.6 and 2.7, their coefficients and their modular ratio (C_L, C_D, $\left|\frac{C_L}{C_D}\right|$).

The physical construction of the model for experimentation required adaptations to laboratory conditions.

4.1 3D Model Projection and Construction

The first step of the entire project was to define which airfoil model would be adopted for experimentation. Such an airfoil should be efficient at a low Reynolds number and have its curvature compliant with the production of downforce. The Eppler family airfoils are historically used in wing analysis in vehicle aerodynamics, as they have a more asymmetrical and more cambered nature, which favors the pressure differential at lower speeds and angles of attack in relation to typical aircraft airfoils. Thus, the chosen airfoil, according to the literature (NAIR, 2014-2015), was the model **e423-il** or simply **E423**, which is a model focused on high lift for less turbulent Reynolds numbers, though with an particularly high C_D.

Thus, through the E423 .dat file (Figure 20), this geometry was imported into a Computer Aided Design (CAD) software, SolidWorks®.

Figure 20 – E423 2D airfoil with axes based on percent dimensionless chord

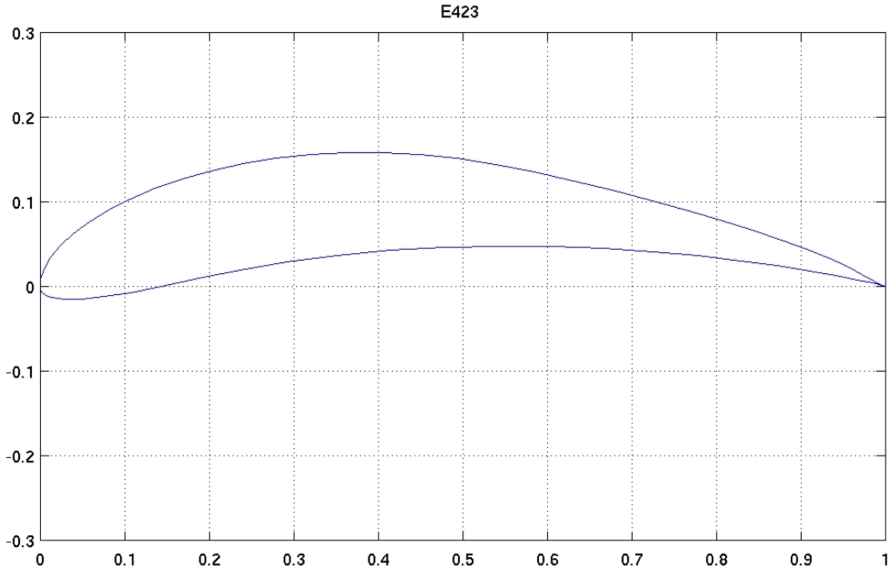

Source: https://m-selig.ae.illinois.edu/ads/afplots/e423.gif

4.1.1 Geometry CAD details

The airfoil's dimensions were defined as the chord measuring 190 *mm* with it's wingpans measuring 500 *mm*.

First, through the website *airfoiltools.com*, it has been imported the airfoil geometry into the CAD software - multiplying the chord value to 190 *mm* - and extruded it to the wingspan size 500 *mm*. However, according to other experiments carried out in the laboratory, since the model will be printed by a 3D printer, its limited size forced to divide the model, the E423 airfoil, into 3 equal parts to be printed separately, as it has no size to print 500 *mm* of wingspan at once. Thus, the longitudinal division into 3 parts of the airfoil was necessary, and each part has a $\frac{500}{3}$ *mm* of wingspan (or $166,67$ *mm* each).

Because of this division, it was necessary to create a geometric device to unite the three parts without any gap or discontinuity in the original geometry of the airfoil as a whole. Then, in each of the three parts of the "semi-airfoils", two holes of 6 *mm* in diameter were drilled so that a solid shaft (billet) of the same dimension passes through each of the two holes, concentrically joining the three parts and eventually forming the piece as a whole. The Figures 21 and 22, respectively, show the CAD models for the middle part and the tip part of the airfoil (both left and right parts are equivalents, so the Figure 22 refers to both parties).

Note in Figure 21b that there is a recess in the center of the middle airfoil. This comes from the need to mount the model downstream of the wind tunnel flow, because it is

Figure 21 – Middle part of the CAD model of the airfoil (with all-through holes)

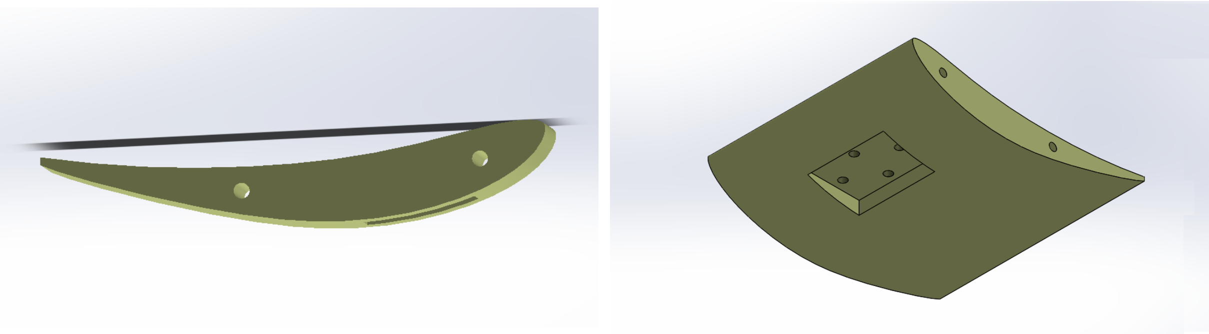

(a) Frontal Vision

(b) Isometric Vision (Detail for the threaded holes)

Source: The Author

Figure 22 – Tip part of the CAD model of the airfoil (with the blind holes halfway down the span)

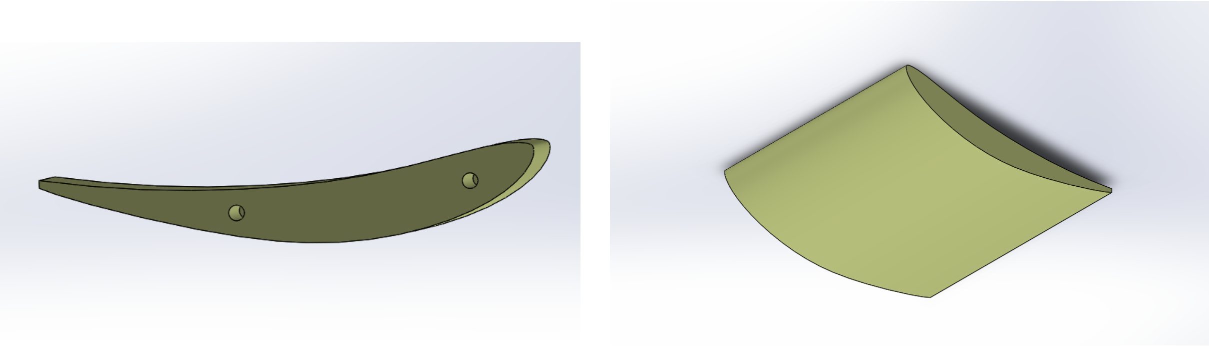

(a) Frontal Vision (blind holes visible)

(b) Isometric Vision (with the back side without the holes)

Source: The Author

necessary to have a rod attached to the airfoil and the aerodynamic balance, completely vertical and rigid, precisely to transfer the load coming from the airfoil perfectly to the balance, accurately confirming the measurement of its forces (see section "aerodynamic balance" for details). In addition, the assembly of the experimental model requires the possibility of varying the height and angle of attack. For the former, firstly, the stem needs to be threaded so that it is possible to vary the height of the airfoil precisely, and it must have a size of the following sum:

$$H_{rod} = h_{hole_{AB}} + e_{TB} + H_{min} \tag{4.1}$$

Where:

- H_{rod} – Total height of the rod;
- $h_{hole_{AB}}$ – Total height of the threaded insert of the aerodynamic scale (AB);
- e_{TB} – Test bench thickness
- H_{min} – Minimum test height of the airfoil in relation to the test bench surface

By manual measurements, considering Figure 31b the total height of the threaded insert of the aerodynamic scale (AB) and the test bench thickness, respectively are $h_{hole_{AB}} = 340\ mm$ and $e_{TB} = 17\ mm$.

To determine the minimum height it must be greater than the thickness of the boundary layer i (Dominy, 1992) formed by the flow on the test bench (δ_{TB}). It can be estimated quite accurately with the following equation (INCROPERA; DEWIT, 2007):

$$H_{min} = \delta_{TB} = 5\sqrt{\frac{\nu x}{v_\infty}} \tag{4.2}$$

Where x is the maximum longitudinal distance over which the runoff can affect, so it can be approximated to the total size of the wing chord $x = c = 200\ mm$. Thus, approximating the speed to the maximum wind tunnel speed (28 m/s) and considering a high temperature of 30ºC, making the coefficient of kinematic viscosity $\nu = 15{,}98 \times 10^{-6}\ m^2/s$; one has $H_{min} \approx 2\ mm$. This value must be added to the minimum height of the experiment, which was defined as the height at which $h/c = 0.1$, so the minimum height at which the airfoil must be in relation to the table surface is 20 mm. So, as per the equation 4.1, $H_{rod} = 377\ mm$.

4.1.2 CAD Assembly

As already mentioned, the experiment needs an assembly of parts in order for the experimentation to be possible and effective. Two of these parts have already been mentioned: the wing and the stem. For the complete assembly, more parts are needed.

- **Two bars:** As already mentioned in the airfoil section, the division into three parts of the airfoil brought the need to join them, and with that the two holes were made in each of the three parts (Figure 23b) that are filled by the billets of $\frac{2}{3}500\ mm$ (or 333.33 mm). Visible in Figure 23d.
- **Fixing Metal Plate:** Made to be fitted by means of 4 screws (model M6 x 1.01 mm) in the middle part of the wing. The recess in it is necessary to disturb the air flow as little as possible. Note in Figure 23a a double shoulder with an M10 through hole; A screw of the same diameter will pass through it for fixing on the rod with the possibility of varying the angle of attack of the airfoil. Detailed dimensions are in the appendix D.
- **Rod fixation on the plate:** At one end of the rod (Figure 23b), there are a hole with an M10 diameter, to pass the same screw mentioned on the fixing plate. The holes in this and

Figure 23 – Assembly parts

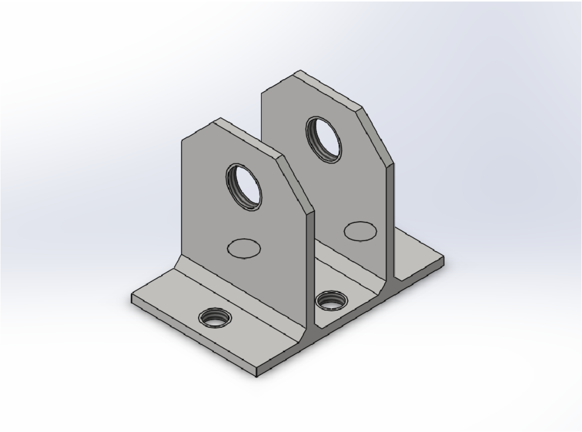

(a) Fixing Plate (Mounted on the middle part of the airfoil)

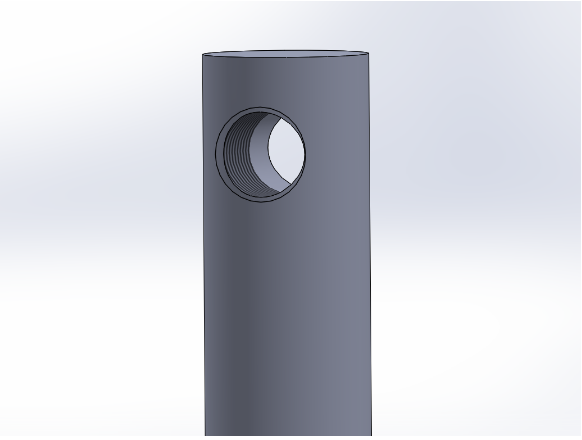

(b) Detail of the rod for fitting to the plate with a screw

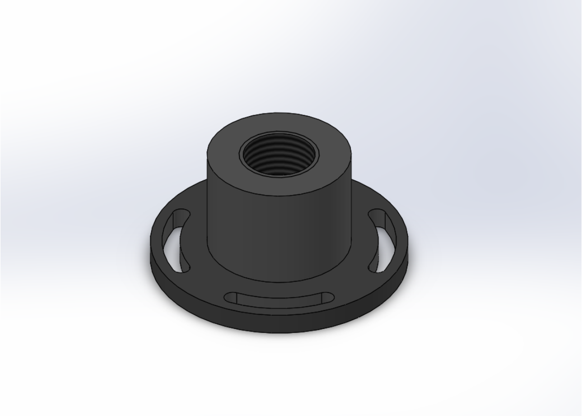

(c) Flange for fitting to the aerodynamic balance

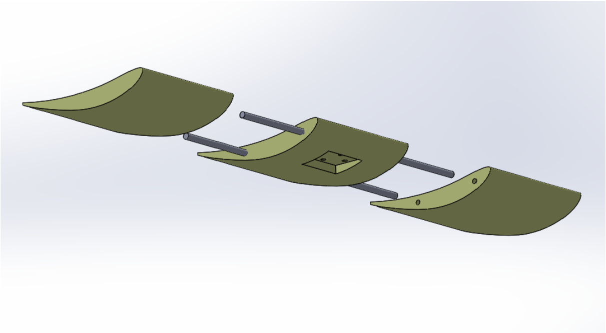

(d) Exploded view of the three parts of the airfoil, with the fitting shafts visible

Source: The Author

the rod are concentric.

- **Flange:** The flange serves to fit the aerodynamic balance, has a 20 *mm* hole (same size as the rod), and its geometry is shown in the Figure 23c. Detailed dimensions are in the appendix C

In this way, the assembly was carried out in the software, shown in the Figure 31. Note that the smaller screws are not shown.

Figure 24 – General Assembly

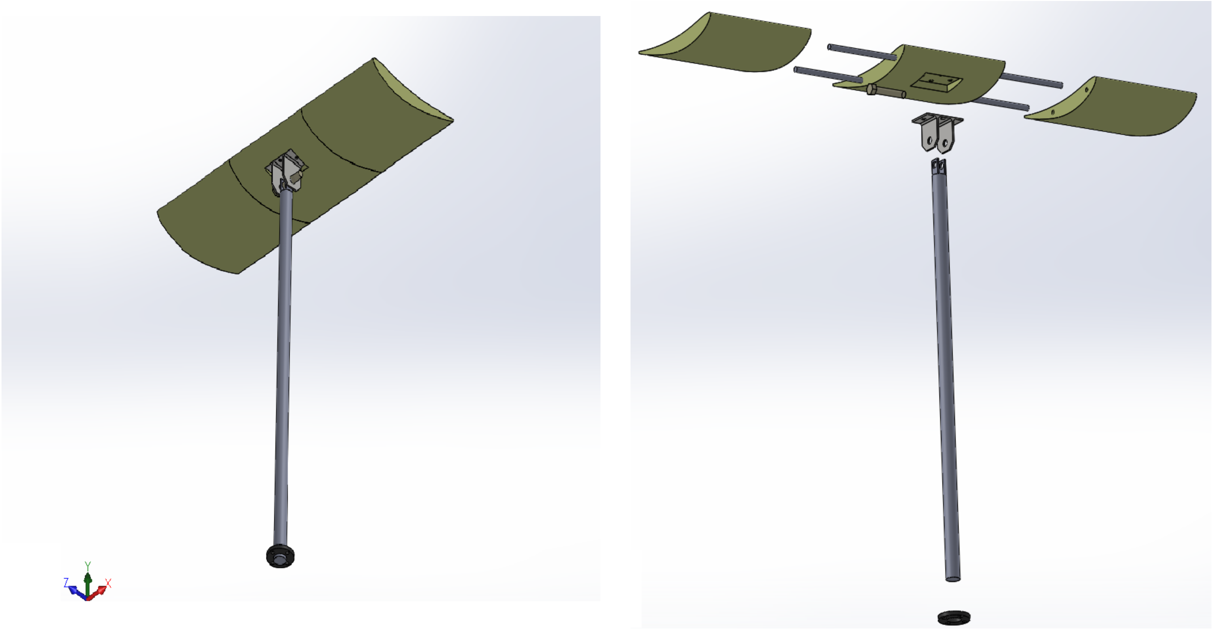

(a) Complete

(b) Exploded view

Source: The Author

4.1.3 Physical construction of the model

As already mentioned in the introduction, the main piece of work, the E423 airfoil, is produced by the rapid prototyping manufacturing process, which basically consists of filaments of PLA (Poly Lactic Acid) of 1.75 in diameter that are successively added layer by layer to create the geometry. The 3D Printer, MakerBot® model (Figure 25a), was used in this process. It is controlled by software of the same brand that allows printing options such as the type of internal structure (diamond, hexagonal, parallelepiped, etc.); the support material, such as the type of ground support; the types of travel moves of the printer; the layer highlights and does a simulation of time and the total material usage of the current project (Figure 25b). In this experiment, the internal geometry used was diamond-shaped type.

The limited size of the 3D printer, which has a maximum print dimension of $(300 \times 305 \times 457\ mm)$ is precisely the reason that the airfoil has to be divided into three parts, since it has a wingspan of 500 *mm*, exceeding any of the printer's spatial limits, in all three dimensions.

As for the other components of the assembly, the rod was purchased ready, being threaded externally to fit the aerodynamic balance; both the flange and the fixing plate were manually manufactured in a workshop following the dimensions of the technical drawing in the appendices C and D, respectively.

The Figure 26 shows some of the finished parts.

Figure 25 – 3D Printer MakerBot® model

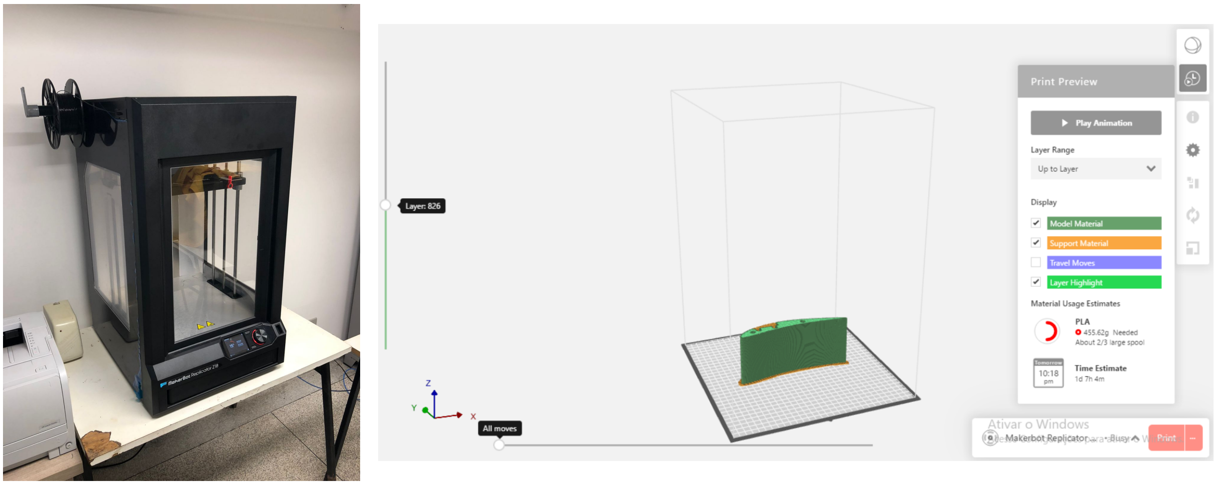

(a) The printer itself

(b) The printer's software interface

Source: The Author

Figure 26 – Finished parts

(a) Fixing Plate

(b) The Airfoil after being sanded and assembled

(c) Flange

(d) The hod (hole details)

Source: The Author

4.1.4 The contruction and the fixing of the endplates

According to the patent (ALLEN, 2001), endplates do not need to be too elaborate or complex for their effects to be relevant to the aerodynamic efficiency of the wing. In this way, a very simple endplate model was built without the help of CAD.

The shape of the endplate would initially be rectangular, but the forward-facing lower edge of the airfoil would touch the ground at very high angles of attack, since, for ground effect, the airfoil is very close to the ground. Thus, this region of the endplate was rounded while the others remained intact. To scale it, an airfoil contour was made on a wooden board to base the contour of the curved front part. Then, the top of the endplate should be long and extrapolated, precisely so that it can effectively block the large wingtip vortices. Figure 27 shows this sketch, with the dimensions in centimeters of the plate.

Figure 27 – Endplate dimensions sketched

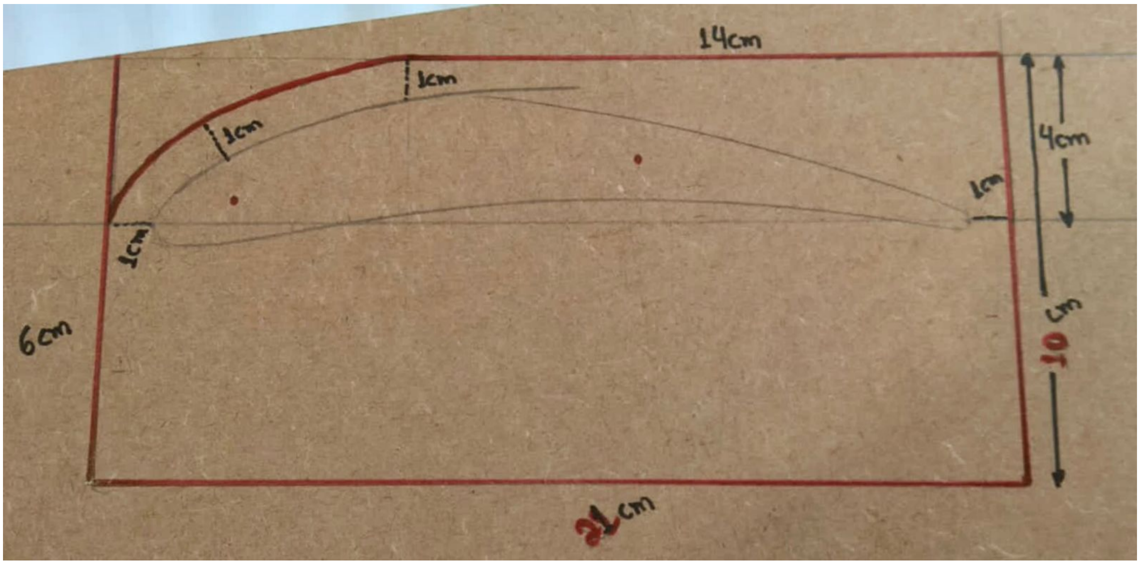

Source: The Author

With these dimensions defined, the acrylic plate was cut (2 *mm* thickness) as the sketch for the endplate to take shape.

Fixing the endplate, being made of acrylic and therefore very light, was also simple: with 2 M4 screws directly on the side of the wing. Figure 28 shows both endplates already mounted on the airfoil.

Figure 28 – Endplates used in the experiment

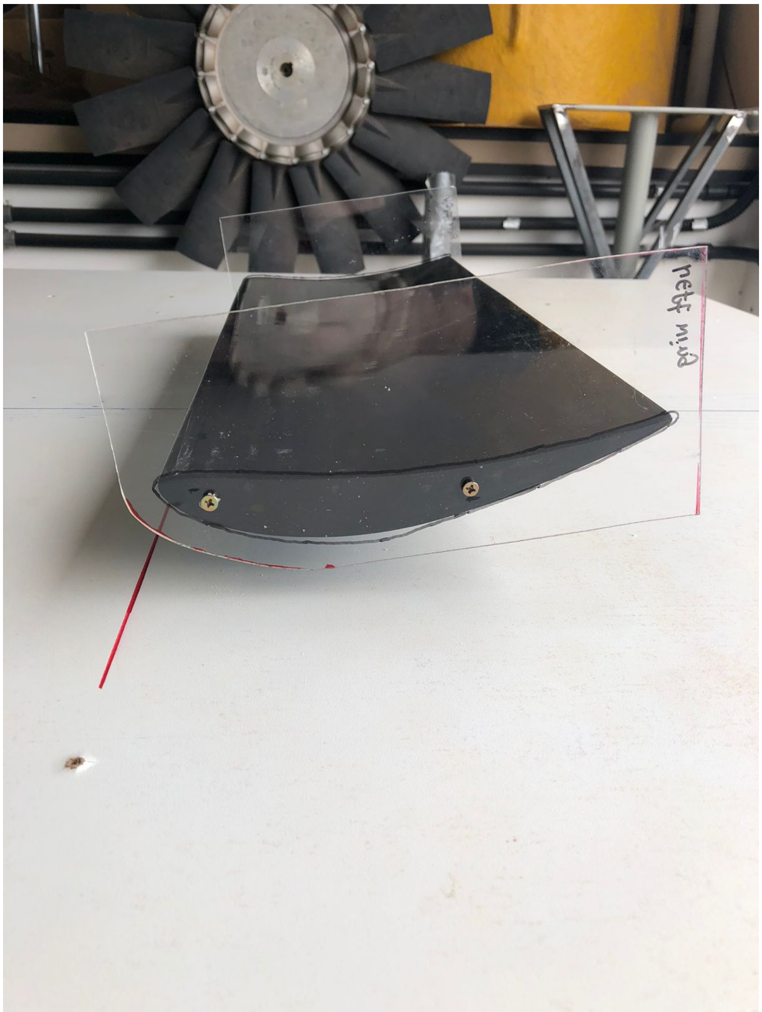

Source: The Author

4.2 Wind Tunnel

The tests were conducted in an open section subsonic wind tunnel called TV60; which belongs to the Experimental Aerodynamics Laboratory (LAEX), as part of Experimental Aerodynamics Research Center (CPAERO), located at the LAEX in building 1DCG of the Federal University of Uberlândia (Campus Glória). The wind tunnel drive system consists of a $25HP/220V$ electric motor, which drives a rotating rotor that moves the air proportionally to its rotational speed in order to produce a flow, whose rotor exit speed is controlled by a frequency 'inverter' (standard for the Brazilian electrical grid, 60 Hz). This system of electrical variation provides the possibility of producing a flow of up to a maximum of 28 m/s.

The actual flow velocity in the wind tunnel is measured by a Pitot Tube (Model Kimo MP 200) connected to a transducer. The ambient temperature, which is important for the correction of the specific mass, ρ, is measured by a thermometer and inserted into the transducer.

Figure 29 – Wind Tunnel TV60 (LAEX/CPAERO -UFU)

Source: The Author

The Pitot Tube is shown at Figure 30.

Figure 30 – Pitot tube

(a) Mounted at the exit of the wind tunnel (b) The interface

Source: The Author

Typically, wind tunnel tests disturb the flow to the point that corrections to the results presented are necessary. However, in this experiment, the airfoil is not inside the closed section of the tunnel, making such corrections unnecessary. Details of these corrections are in Appendix B, which details fixes for the solid Blockage, the wake blockage, and the streamline curvature.

4.3 Balance of aerodynamic forces

The aerodynamic balance used in the experiment is an external balance developed to measure three aerodynamic components: normal force (lift), axial force (drag) and lateral force, in addition to measuring the fundamental momentum of flight: roll, pitch and yaw.

Figure 31 – Aerodynamic balance - AA-TVAB2®

(a) Bottom part

(b) Upper part

Source: The Author

It can be seen in Figure 31b, the circular fitting has the characteristic shape of the flange (Figure 23c). It is there that the fitting of it with the rod occurs, and that determined the size of $h_{hole_{AB}}$. Since the aerodynamic balance measures the forces, they are interpreted by the software of the same company, whose interface is shown in the Figure 32.

4.4 Experimental procedure

In order to measure and characterize the lift and drag on the airfoil, the aerodynamic balance connected to the wind tunnel was used, and the airfoil was connected to it, through the rod, which transfers the forces suffered by the wing. Before the experiment, the balance was calibrated to assess lift force, using standard masses which were added to the balance axis, thus

Figure 32 – Software screen (AA-TVAB2®)

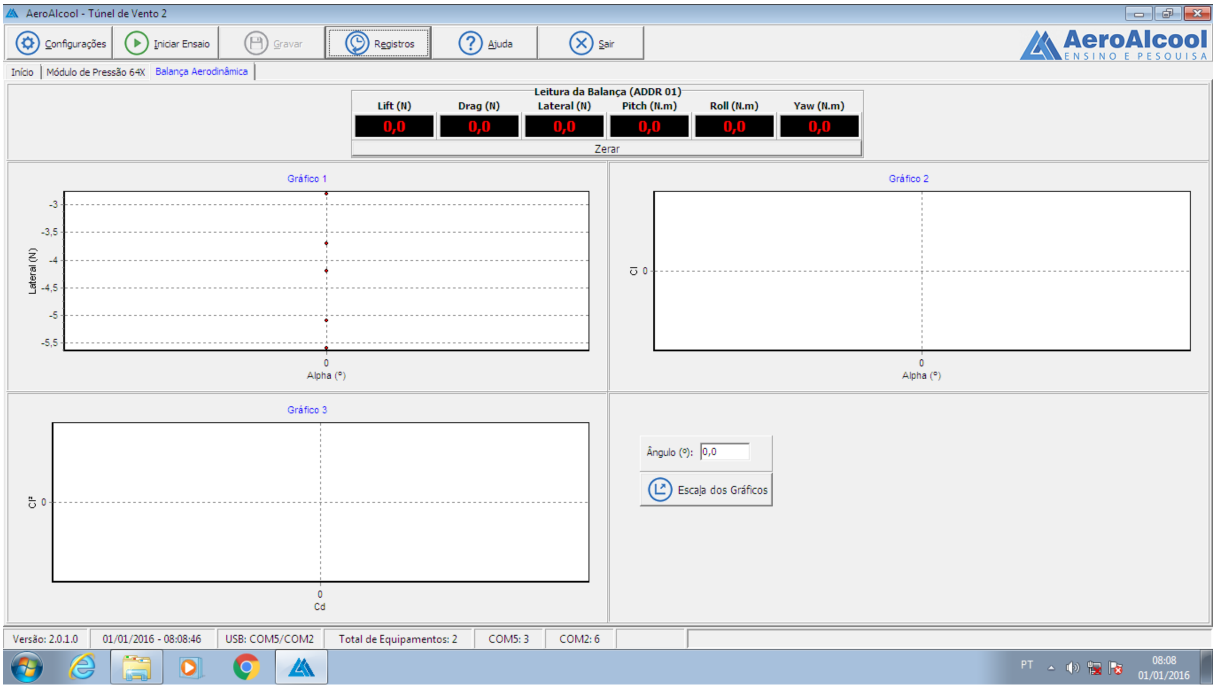

Leitura da Balança (ADDR 01)

Lift (N)	Drag (N)	Lateral (N)	Pitch (N.m)	Roll (N.m)	Yaw (N.m)
0,0	0,0	0,0	0,0	0,0	0,0

Ângulo (°): 0,0

Versão: 2.0.1.0 | 01/01/2016 - 08:08:46 | USB: COM5/COM2 | Total de Equipamentos: 2 | COM5: 3 | COM2: 6

Source: The Author

simulating the maximum load supported by the model. This procedure is performed so that the data provided by the balance present adequate results in the context of the measurements.

As for the wind tunnel, it works by an inverter that, at a certain frequency, drives a certain speed. Thus, also before the experiment, the tunnel was calibrated in order to establish the flow velocity as a function of the established frequency. For this experiment, a fixed velocity (and therefore a fixed Reynolds number) of 22 m/s was established, which, thanks to calibration, corresponded to a standard frequency of $50,20$ Hz.

Starting the experimental procedure, the initial conditions are first established. First of all, it was done:

- The computer coupled to the aerodynamic balance was turned on, and the aerodynamic force data acquisition software was initialized (Figure 32);
- The values of pressure and ambient temperature (taken in the morning and afternoon of two different days) were recorded;
- The ambient temperature value was adjusted in Kimo MP 200 so that the pitot tube measures the flow velocity correctly;
- The entire assembly of Figure 31 was fixed to the scale (remembering that the height of the rod and the angle of the wing are variable);
- Both the wing and the pitot tube were aligned perpendicular to the flow.

The balance interface, shown in Figure 32, demonstrates the measurement of aerodynamic forces in real time, and for measuring lift, it has a resolution of $1,7$ N and $0,1$ N for drag. Because the resolution is somewhat low for the lift force, a lot of measurements were made in order to follow the metrology principles and thus to take the average between them and then to guarantee more precision. The sequence of the experimental test was as follows:

1. A certain condition of height and angle of attack is fixed for the airfoil;
2. The balance is zeroed;
3. The wind tunnel is turned on;
4. The wind tunnel is expected to reach the test speed (which is monitored according to the pitot tube);
5. The measurement starts, which saves the instantaneous force values every $0.2s$;
6. It takes around 60 seconds to collect around 300 data samples;
7. Save this data in a spreadsheet and turn off the wind tunnel;
8. Repeat the process for the same wing condition two more times, totaling three sets of samples;
9. The airfoil condition is changed and this process is carried out for it, returning to step 1.

Figure 33 demonstrates the finished experiment, with the airfoil positioned 510 *mm* in front of the wind tunnel exit and fixed to the rod, which is fixed to the aerodynamic balance that is below the test table. Note the left half of the Figures without endplates and the right half with the presence of the endplates.

4.4.1 Test division

The essays of this work were divided in two in order to better organize the objectives and the results of the work. In both tests the airfoil was positioned at 510 *mm* from the wind tunnel exit and the same tunnel speed (22 m/s) was used.

- **Test 1: Variation of height and angle of attack (without endplates)**

  Being a test made to evaluate the relationship not only of the height in relation to the ground, but also of the angle of attack of the airfoil; two heights were selected from the ground, one that would not be subject to the ground effect and another that would be: 300 *mm* ($h/c = 1,5789$) and 38 *mm* ($h/c = 0,2$). For each of these heights, five characteristic angles of attack (0°, 4°, 8°, 12° and 14°) were evaluated, in order to understand aspects such as maximum ratio $\left|\frac{C_L}{C_D}\right|$ and stall angle.

Figure 33 – Assembly ready for experimentation, with different conditions

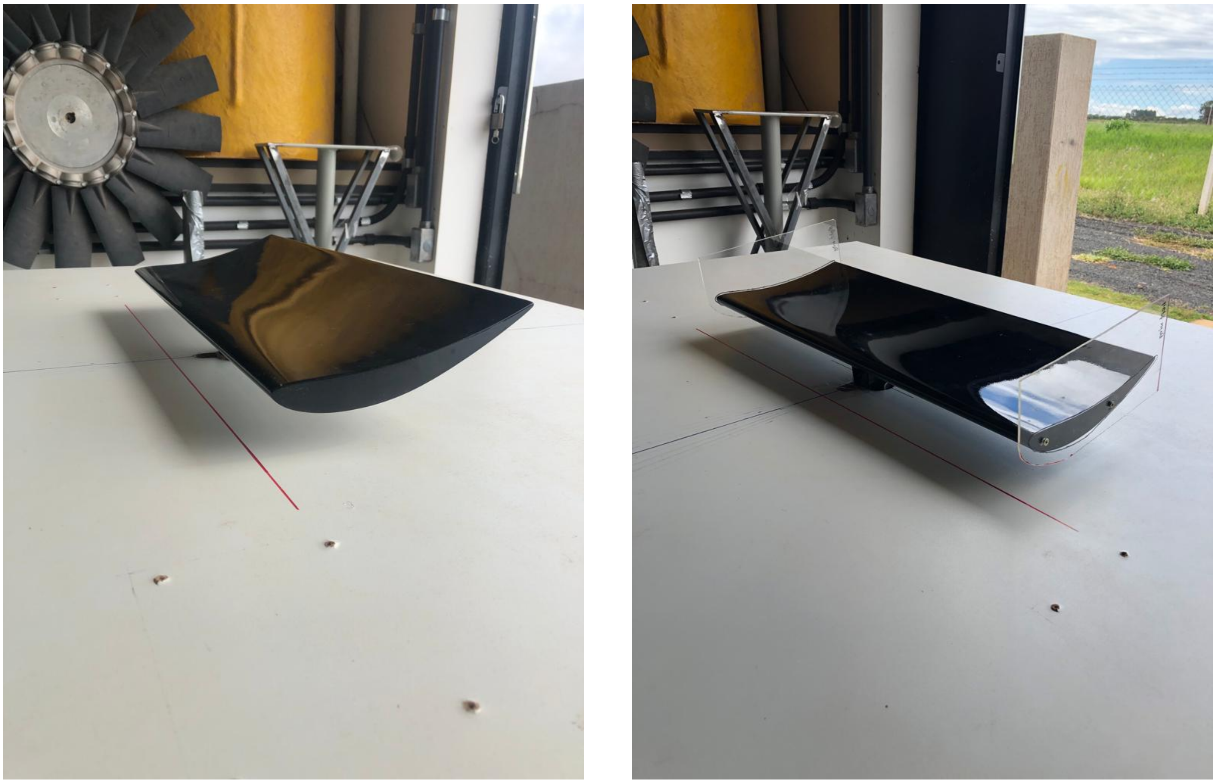

(a) Wing assembly without endplate, viewed from the side

(b) Wing assembly with endplate, viewed from the side-front

(c) Wing assembly without endplate, viewed from the back-left

(d) Wing assembly with endplate, viewed from the back-right

Source: The Author

- **Test 2: Variation of height and presence of endplates (with fixed α)**

  In order to reproduce and evaluate the Katz experiment (KATZ, 2006), especially the graph in Figure 15, for an different and a more cambered airfoil with a greater angle of attack. This angle was set at $\alpha = 8^\circ$ and the height from the floor (to the table of assay) in values of: $h_1 = 38\ mm$ $(h/c = 0,2)$; $h_2 = 56\ mm$ $(h/c = 0,2947)$; $h_3 = 75\ mm$ $(h/c = 0,3947)$; $h_4 = 94\ mm$ $(h/c = 0,4947)$; $h_5 = 113\ mm$ $(h/c = 0,5947)$; $h_6 = 135\ mm$ $(h/c = 0,7105)$; $h_7 = 154\ mm$ $(h/c = 0,8105)$; $h_8 = 171\ mm$ $(h/c = 0,9)$ and $h_9 = 190\ mm$ $(h/c = 1,0)$. In addition, for each height, the test was performed with and without endplates. The objective of this is to quantitatively analyze the combination of ground effects and the presence (or not) of endplates on the wing, focusing on lift and drag.

5 RESULTS

After all the theoretical preparation, with foundations and bibliographic reviews, together with the assembly of the practical experiment; the results were computed.

5.1 XFRL5® SIMULATIONS

First, for a basis of comparison, the software XFRL5® was used, in order to verify the fidelity of the experimental analyzes carried out in this work, with numerical data of the behavior of the two-dimensional flow. It stands out for its consistency and ease of operation, in addition to being a free program. Such software is a computational tool capable of providing coherent analyzes in the support and control predictions, in addition to, mainly, providing the curves as a function of α for a certain Reynolds number. Since the coefficients change with the angle of attack, it is vitally important to look at the graphs of these coefficients, such graphs are called polar aerodynamics. The aerodynamic coefficients are used to preliminary evaluate the performance of the profiles

The XFLR5® (XFRL5. . . ,), however, does not have simulation for ground obstacles or any solid additions to the wing, that is, it only evaluates a 2D profile under free airflow of obstacles and external forces such as gravity; it is only necessary to load the model, establish the flow Reynolds number (fixed) and evaluate graphs according to the angle of attack. Because this work is purely experimental, the graphs of Figure 34 serve as a basis for the behavior of the airfoil under ideal conditions, not only free flow, but also free of obstacles, with disregard for physical parameters such as viscosity, rotation, entropy or even gravity. This simulation, therefore, is very useful to compare with the first part of test 1, the one with the airfoil positioned at a dimensionless distance of $h/c = 1.5749$, since in this position there is no interference from the ground or endplate.

Thus, the first step is to calculate a very accurate estimate of the Reynolds number present in the experiment, according to the equation 2.4. The wind tunnel speed has been adjusted with 22 m/s with a mean of temperature in the laboratory of 27ºC, making the coefficient of kinematic viscosity $\nu = 15,80 \times 10^{-6}\ m^2/s$, and the length L as the chord of the airfoil ($c = 190\ mm$), the uncorrected Reynolds number is:

$$Re = 265760$$

Note that Re is within the order of magnitude reported as a low Reynolds number (WINSLOW J.; OTSUKA, 2017): 10^5

Because the simulation does not consider the wind tunnel, the corrections are not necessary in this case. Calculating the Reynolds number, it was fixed and the angle of attack was varied from -10° to 18° in order to plot the following graphs for the 2D-E423: $C_l \times \alpha$ (34a); $C_d \times \alpha$ (34b); $C_m \times \alpha$ (34c) and $\left|\frac{C_l}{C_d}\right| \times \alpha$ (34d). All following graphs have degree as the unit of α.

Figure 34 – E423 Graphs for XFRL5® software ($Re = 265760$)

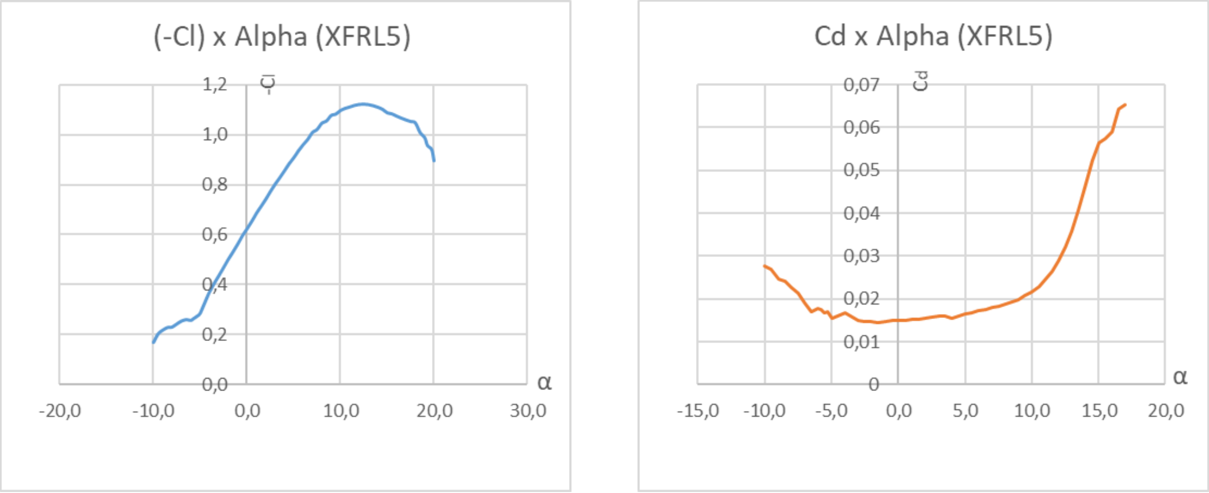

(a) $C_l \times \alpha$ graph

(b) $C_d \times \alpha$ graph

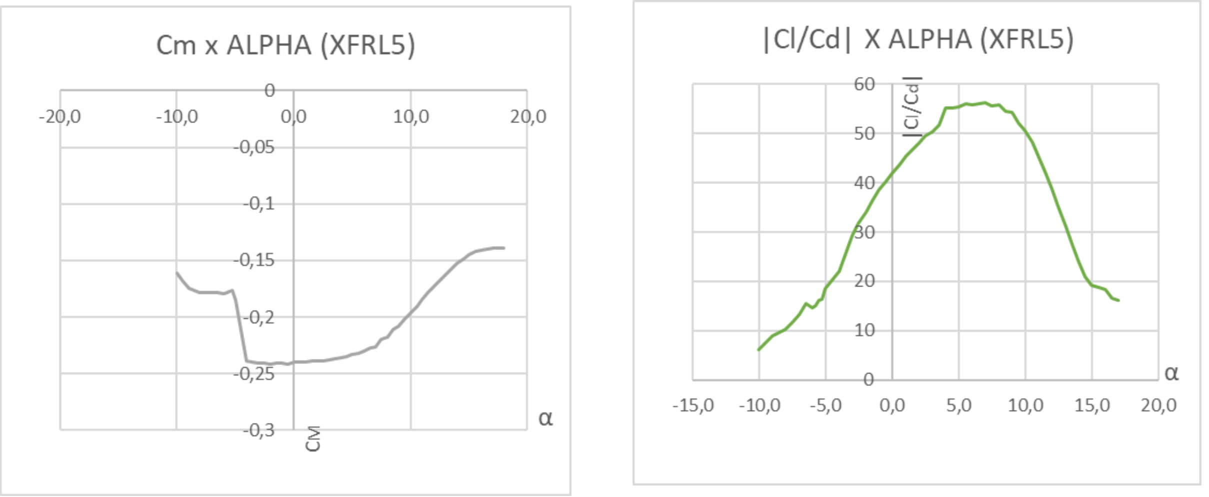

(c) $C_m \times \alpha$ graph

(d) $\left|\frac{C_l}{C_d}\right| \times \alpha$ graph

Source: The Author

5.2 Results for test 1

As test 1 consists of an evaluation of downforce (a.k.a. negative lift) and drag as a function of the angle of attack with and without the airfoil being subjected to ground effect, the results were computed. Remembering that for all tests, the flow velocity is fixed as 22 m/s. Remembering too that the standard Cartesian axes are used for the principles of applied aerodynamics: lift has a positive upward direction and drag has a positive direction against the flow movement. Therefore, the values of L and C_L tend to be negative since the airfoil is for downforce producing. The tables 1 and 2 summarize the results obtained for the height $h/c = 1.5737$ which, theoretically, does not suffer ground effect; showing collected aspects such as the pure average of the lift and drag force, their respective coefficients and the standard deviation (σ) for the measurements, as a function of the attack angles.

α	L	C_L	$\sigma(L)$
0°	$-3,8132\,N$	-0,1398	1,3560
4°	$-13,2745\,N$	-0,4865	1,3956
8°	$-21,7587\,N$	-0,7975	1,3543
12°	$-23,7345\,N$	-0,8699	1,6243
14°	$-21,5455\,N$	-0,7897	1,3272

Table 1 – Lift results for test 1 at $h/c = 1.5747$

α	D	C_D	$\sigma(D)$
0°	$5,0331\,N$	0,1845	0,9345
4°	$3,2465\,N$	0,1190	0,7712
8°	$3,4029\,N$	0,1247	0,6932
12°	$4,5151\,N$	0,1655	0,7847
14°	$6,2737\,N$	0,2299	0,7981

Table 2 – Drag results for test 1 at $h/c = 1,5747$

Chronologically, the first test to be done was with the height at half the height of the wind tunnel, resulting in $h/c = 1.5749$, during the afternoon of a humid day (average of 76% humidity) , with an average temperature of $26.7°C$, with a relatively low wind speed ($2,83$ m/s) which can influence the wind tunnel flow, since, as it can be seen in Figure 33, tunnel runoff exits to an outdoor area. For this part of the test, the Reynolds number is $Re = 266945$.

Following the time, it was made, still in the test 1, the variation of the angles of attack to $h/c = 0,2$ in the morning of the following day (results in tables 3 and 4). Atmospheric

α	L	C_L	$\sigma(L)$
0°	$-9,1556\,N$	0,5201	1,3621
4°	$-10,0990\,N$	0,6311	0,9909
8°	$-10,3261\,N$	0,7119	1,0118
12°	$-12,5284\,N$	0,8455	1,3392
14°	$-23,7479\,N$	1,0010	1,2860

Table 3 – Lift results for test 1 at $h/c = 0,2$

α	D	C_D	$\sigma(D)$
0°	$2,4335\,N$	0,1305	0,7116
4°	$2,7344\,N$	0,1243	0,4727
8°	$2,2713\,N$	0,1616	0,4719
12°	$4,0620\,N$	0,2123	0,8573
14°	$0,3983\,N$	0,0912	1,7663

Table 4 – Drag results for test 1 at $h/c = 0,2$

conditions were already relatively different: average test temperature of $25,2°C$, high humidity $(88,3\%)$, and especially with a higher wind speed: $6,16\ m/s$. All this must be taken into account not only for calculating the number of Reynolds, which directly impacts the calculation of the coefficients C_L and C_D, according to the equations 2.6 and 2.7; but also to assess the principles of sources of error. For this part of the test, the Reynolds number is $Re = 268810$.

For a better visualization, the graphs $C_L \times \alpha$ and $C_D \times \alpha$ were plotted for test 1, shown in the Figures 35 and 36, respectively.

First, analyzing the Figure 35, it is noted that, for the purpose of comparing the highest height (without ground effect) and the data collected in XFRL5, the lift (downforce) curve is practically parallel shifted downwards. This can be explained by the fact that the lift coefficient of a wing is always will be lower than that calculated for the profile, due to the lower capacity to generate wing support, in relation to the 2D-profile (RAYMER, 1992). This effect is noticeable when analyzing the $C_{L_{max}}$, which even with this deviation occurs at practically the same angle of attack for both experimental and XFLR5 data: $\alpha_{C_{L_{max}}} \approx 12°$. After this angle, the lift coefficient begins to drop, referring to the stall effect. This proves that, in this case of the dimensionless height of $h/c = 1.5747$, this part of the experiment had great precision.

Comparing now the data of $h/c = 1.5747$ and $h/c = 0.2$ for support, a very noticeable deviation was noticed. For the smallest angles of attack, precisely the angles of 0° and 4°, the lift coefficient for the wing under ground effect was significantly higher, as expected by the ground effect theory. However, this behavior is not seen for the two subsequent angles, which had a

Figure 35 – $-C_L \times \alpha$ for the first test

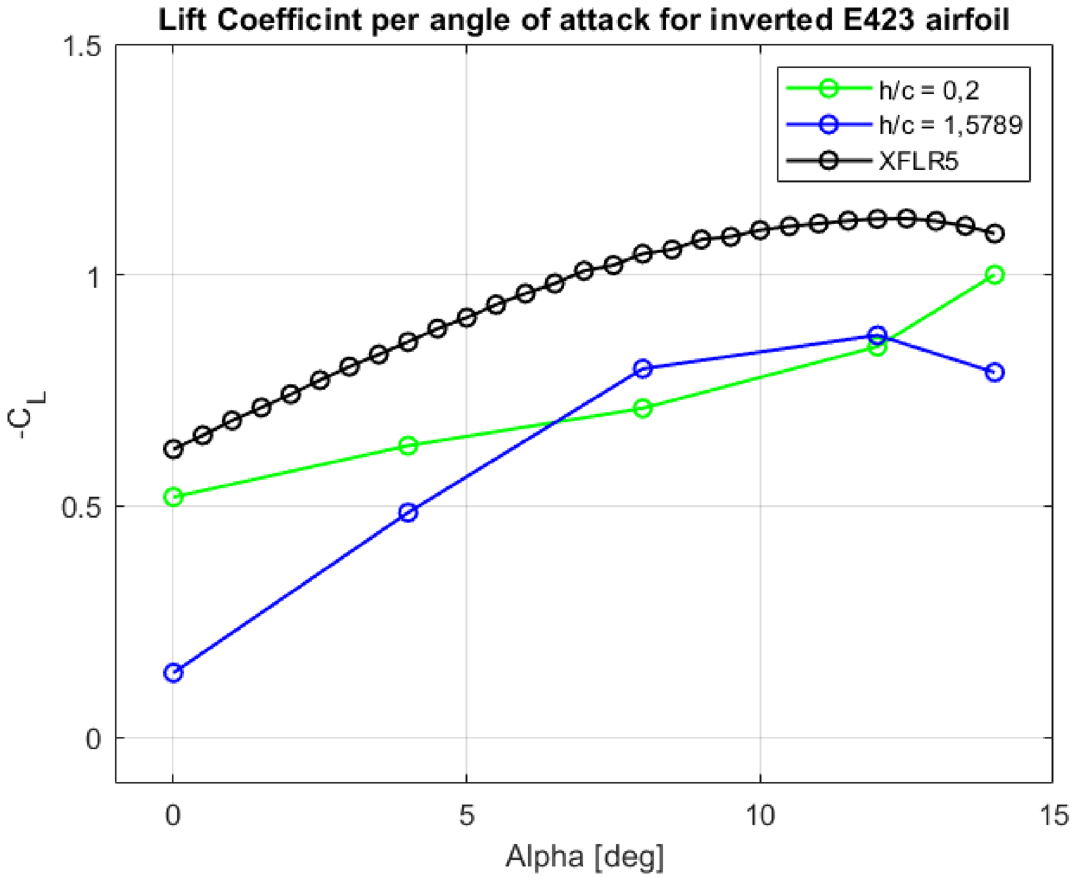

Source: The Author

slightly lower lift coefficient compared to the same for the highest height. A plausible explanation for this effect comes from looking at the value of C_L for 14°, which reduces for greater height and remains with a tendency to increase when the wing is in ground effect. Since the ground effect, by its nature, prevents the vortices from completing, this ends up causing a reduction in the turbulence characteristic and possibly increasing the stall angle, going, however, completely against the theory (SKYBRARY, 2012) seen in the Figure 14. However, the theory considers aircraft wings first, not race car wings, which tend to face a flow in the order of magnitude of Reynolds $10^6 - 10^7$. And noting the work of literature (KATZ, 2006) and (ZERIHAN, 2001), both used in their experiments a Reynolds number of the order of magnitude of 10^6, while the present work was done under a Reynolds number of 10^5. As the other tests had a higher precision, one cannot consider only the experimental errors, it can be concluded that the low Reynolds inherent to the laboratory made the viscous effects more relevant, which compromises the performance of the wing, especially in terms of C_L, harming even more under ground effect, in which the higher speed on the soffit of the wing causes a greater acceleration of the flow and, according to viscosity theory, increases these effects. And such acceleration in the flow is intuitively greater for the larger angles of attack, which must have caused a bubble of air recirculation in this region close to the ground, with a velocity not high enough to have energy to break this effect which, due to limited laboratory equipment, it was not possible to investigate the larger Reynolds, which paves the way for future investigations into this effect. Therefore, in this case, the wing will have a more efficient C_L for larger angles if the Reynolds number is greater, sometimes increasing the speed, sometimes increasing the size of the airfoil, whose wing dimensions in this work are in smaller proportions than the airfoils used in racing cars (see Figures 5 and 6).

Figure 36 – $C_D \times \alpha$ for the first test

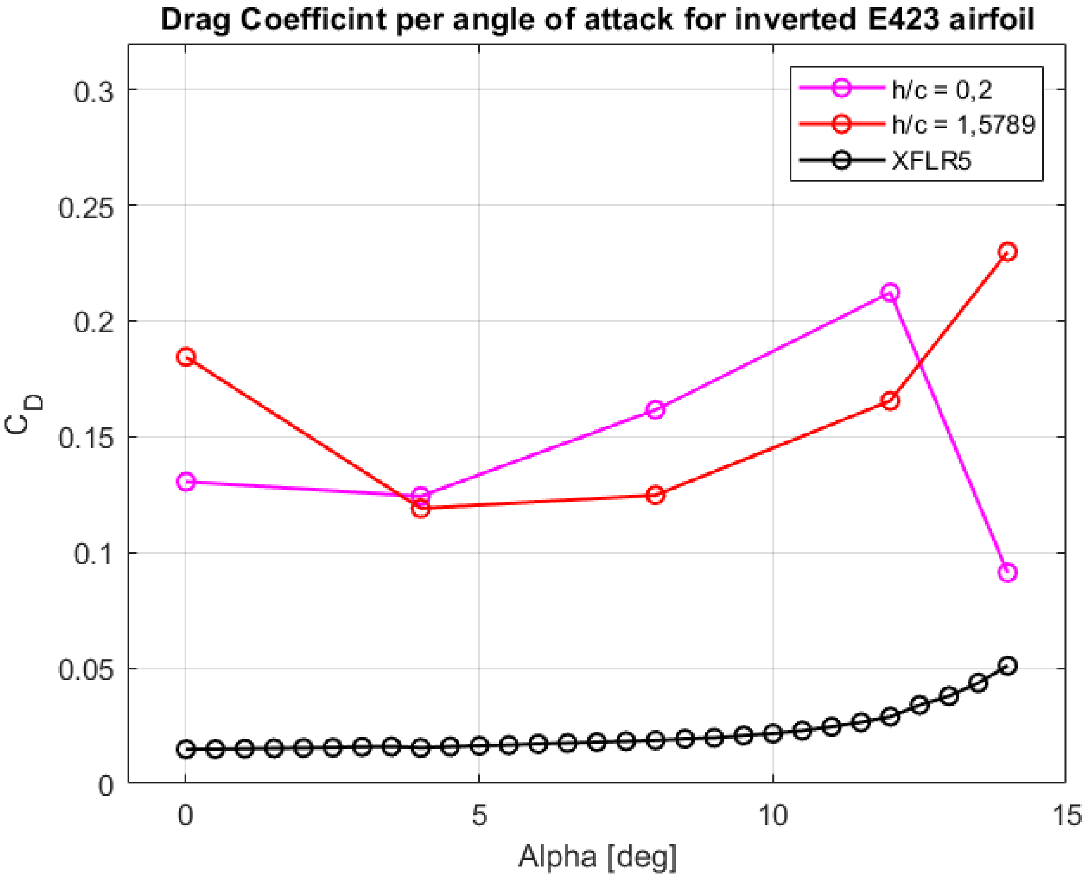

Source: The Author

The first thing to note in the drag coefficient plot (Figure 36) is that, compared to the XFRL5 data, both experimental data had much higher drag. This is due to an inherent condition arising from the choice of the assembly the test model of the experiment: the presence of the rod (Figure 23b) connecting the wing to the aerodynamic balance. The stem ends up in the flow path as does the wing (Figure 33), and therefore is subject to the same air flow, contributing to all measurements, especially drag. As the rod connected the airfoil through the sheet metal (Figure

23a), making this also having a negative effect on the drag. As the height increased, more of the rod was subjected to drag, of parasitic nature.

As for the evolution of the angle of attack and the comparison between the two heights, a similar problem with the downforce was encountered: the viscous effects and the possibility of a recirculation bubble present in the airlow results. Again, for the first two angles, the logic is confirmed: the lower height in relation to the ground causes less drag thanks to vortex interruptions; however, the low value of Re caused the recirculation bubble that destroyed the airflow in the underside of the wing, and recirculations, according to theory, increase the C_D. As for the extraordinary value of C_D to $\alpha = 14^\circ$, this was due to the extreme proximity of the front part of the airfoil in relation to the other angles, practically touching the test table, which greatly reduced the airflow in the rod, reducing the drag and also the measurement accuracy. This also explains the growth of C_L in this region at $h/c = 0.2$. Therefore, it is a value that is somewhat outside the confidence interval as it can be seen the high standard deviation for the 14° measures in the tables; so this abrupt decrease in total drag could have just been a measurement error or it could actually have been a big change in aerodynamic behavior under these conditions, which can be used for a future investigation in correlation with the observations regarding the tests for $alpha = 14^\circ$ and $h/c = 0,2$.

5.3 Results for Test 2

The main objective of test 2 is to reproduce Katz's experiment (KATZ, 2006) for another airfoil (E423), with a different Reynolds number and different angle of attack, the graph in Figure 15; however, with something more: to compare the behavior of C_L and C_D as a function of the height above the ground, with and without the presence of endplates in the airfoil.

The entire test 2 was carried out in an entire afternoon of just one day, following all the steps present in the methodology. The temperature averaged $26^\circ C$, the humidity were high (average 81%), and very little wind (max $4,3\ m/s$); being very favorable conditions for a good accuracy of the experimentation. That resulted in $Re = 267825$.

The results tables, with the real distance, dimensionless distance, average of the lift/drag force among the hundreds of measurements for each case, their respective coefficients and standard deviation; follow below (tables 5, 6, 7 and 8) with both the presence and absence of endplates.

With these data collected and organized, it was plotted: $-C_L \times h/c$ (Figure 37),

h	h/c	L	C_L	$\sigma(L)$
38 *mm*	0,2000	-19,4234	-0,7119	1,4455
56 *mm*	0,2947	-24,5941	-0,9014	1,4572
75 *mm*	0,3947	-26,1836	-0,9596	1,8631
94 *mm*	0,4947	-25,1920	-0,9233	2,0312
113 *mm*	0,5947	-23,4653	-0,8600	1,4400
135 *mm*	0,7105	-23,6827	-0,8680	1,6170
154 *mm*	0,8105	-23,0031	-0,8431	2,1011
171 *mm*	0,9000	-22,2641	-0,8160	2,1785
190 *mm*	1,0000	-22,8151	-0,8362	1,6277

Table 5 – Lift results for test 2 at $\alpha = 8^\circ$, without Endplates

h	h/c	D	C_D	$\sigma(D)$
38 *mm*	0,2000	4,4366	0,1626	0,6742
56 *mm*	0,2947	4,5384	0,1663	1,0396
75 *mm*	0,3947	4,4829	0,1643	0,6562
94 *mm*	0,4947	4,4807	0,1642	1,0706
113 *mm*	0,5947	4,4924	0,1646	0,7191
135 *mm*	0,7105	4,6809	0,1716	1,3147
154 *mm*	0,8105	4,5993	0,1686	1,0050
171 *mm*	0,9000	5,0065	0,1835	0,7809
190 *mm*	1,0000	4,9825	0,1826	1,2821

Table 6 – Drag results for test 2 at $\alpha = 8^\circ$, without Endplates

h	h/c	L	C_L	$\sigma(L)$	Growth in $-C_L$
38 *mm*	0,2000	-21,6402	-0,7931	1,5865	11,41%
56 *mm*	0,2947	-28,2865	-1,0367	2,0017	15,01%
75 *mm*	0,3947	-28,0974	-1,0298	1,6147	7,31%
94 *mm*	0,4947	-27,0992	-0,9932	1,7364	7,57%
113 *mm*	0,5947	-24,7625	-0,9076	2,4956	5,53%
135 *mm*	0,7105	-25,1690	-0,9225	2,1629	6,28%
154 *mm*	0,8105	-24,0855	-0,8827	1,9642	4,71%
171 *mm*	0,9000	-24,3216	-0,8914	1,9541	9,24%
190 *mm*	1,0000	-23,3480	-0,8557	1,6718	2,34%

Table 7 – Lift results for test 2 at $\alpha = 8^\circ$, with Endplates

$C_D \times h/c$ (Figure 38) and $\left|\frac{C_L}{C_D}\right| \times h/c$ (Figure 39).

Perhaps the main objective of the present work is the evaluative graph of C_L in relation to the degrees of ground effect (that is, the height in relation to the ground) present in Figure 37 and to compare it to the behavior evidenced by Katz, whose different conditions of experimentation have already been raised previously.

Evaluating first the evolution of C_L in relation to the height of the wing, a good

h	h/c	D	C_D	$\sigma(D)$
38 mm	0,2000	4,2935	0,1574	0,6401
56 mm	0,2947	4,2597	0,1561	0,7978
75 mm	0,3947	4,3190	0,1583	1,2028
94 mm	0,4947	4,2566	0,1560	0,8972
113 mm	0,5947	4,6138	0,1691	1,5483
135 mm	0,7105	4,6171	0,1692	0,7541
154 mm	0,8105	4,7714	0,1749	0,8764
171 mm	0,9000	4,8023	0,1760	1,0175
190 mm	1,0000	4,8560	0,1780	0,8728

Table 8 – Drag results for test 2 at $\alpha = 8°$, with Endplates

Figure 37 – $-C_L \times h/c$ for the second test

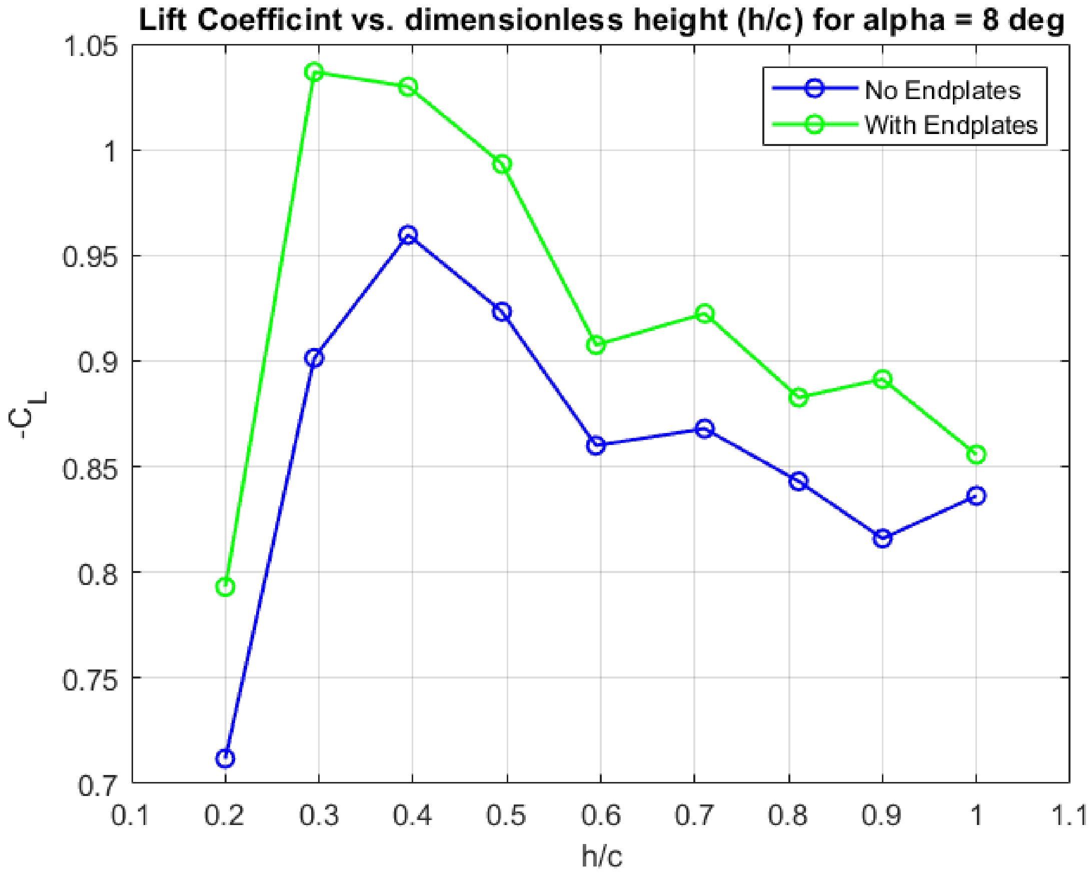

Source: The Author

correspondence with the trend shown by Katz is observed: for height very close to the ground (in the case of $h/c = 0,2$), the C_L is quite low for both conditions evaluated; then it grows a lot, reaching a peak around $h/c = 0,3 - 0,4$ and slowly decays as the values of h/c increase. Intuitively, using the ground effect theory, the closer to the ground, the higher the C_L, and this is confirmed by bringing the airfoil closer to the ground up to $h/c \approx 0.3$. However, as with the Katz experiment, regions extremely close to the ground tend to greatly reduce the C_L because for that regions, the downforce would be limited by viscous effects; being, therefore, exactly the same reasons and consequences enumerated in test 1 (for the distance of $h/c = 0,2$) that the C_L is reduced so much; In addition to the following fact: The presence of the endplate causes that, even with an angle smaller than 14°, there is that effect that there is a solid middle almost touching the ground, which reduces the C_L and tends to also reduce the C_D. This causes the downforce peak with endplates to be at a lower height than without endplates.

It is possible to see that while Katz's experiment (Figure 15) peaks C_L at $h/c \approx 0,15$; in this experiment such a peak varies about $h/c \approx 0,3$. The reason for this comes from the nature of the E423: a very cambered airfoil (see Figure 20), with the chord line passing through it, consequently increasing the absolute value of the height as it is measured up to half of its maximum thickness, which is in one of the vertically rearmost parts of the airfoil: at 31% from the chord.

As for the presence of endplates, there was an optimization in the value of C_L: at all times there was an increase in this value, as is easily visible such gain in support by the graph $-C_L \times h/c$ (the particular percentage of each of the heights is present in table 7). an endplate has the ability to reduce the drag generated by vortices at the wing tip, as it is a plate parallel to the longitudinal axis of the car on which the wing is attached, which manages to constrain the flow and consequently, by the inherent relationship between C_L and C_{D_i} (induced drag coefficient); causes C_L to increase with its presence. Therefore, the theory of endplate performance, explained in the theoretical foundation section, had a precise confirmation in this experiment.

As for the drag (Figure 38), it is possible to notice a problem similar to that of test 1 regarding the presence of the rod, which is less and less "submerged" as the height increases in relation to the test bench. Thus, the greater the height, the greater the parasitic drag caused by the rod. This implies that it is not possible to accurately observe the supposed decrease in C_{D_i} as the height decreases, as this fact constantly increases the total drag (by increasing the parasitic drag).

However, despite this problem, it is possible to draw certain conclusions from the graph. A lower C_D can be concluded in general for the use of endplates in relation to the wing without them (except for some values, which are with high standard deviation, such as $h/c = 0.6$). Theoretically, due to the physical presence of the endplates without any aerodynamic function, the drag should be greater in this case due to the increase in parasitic drag. But precisely because the endplates reduce wingtip vortices (TOET W.; ZERIHAN, 2006), the C_{D_i} is smaller; this proves that the induced drag is actually reduced with the presence of these plates, as per the

Figure 38 – $C_D \times h/c$ for the second test

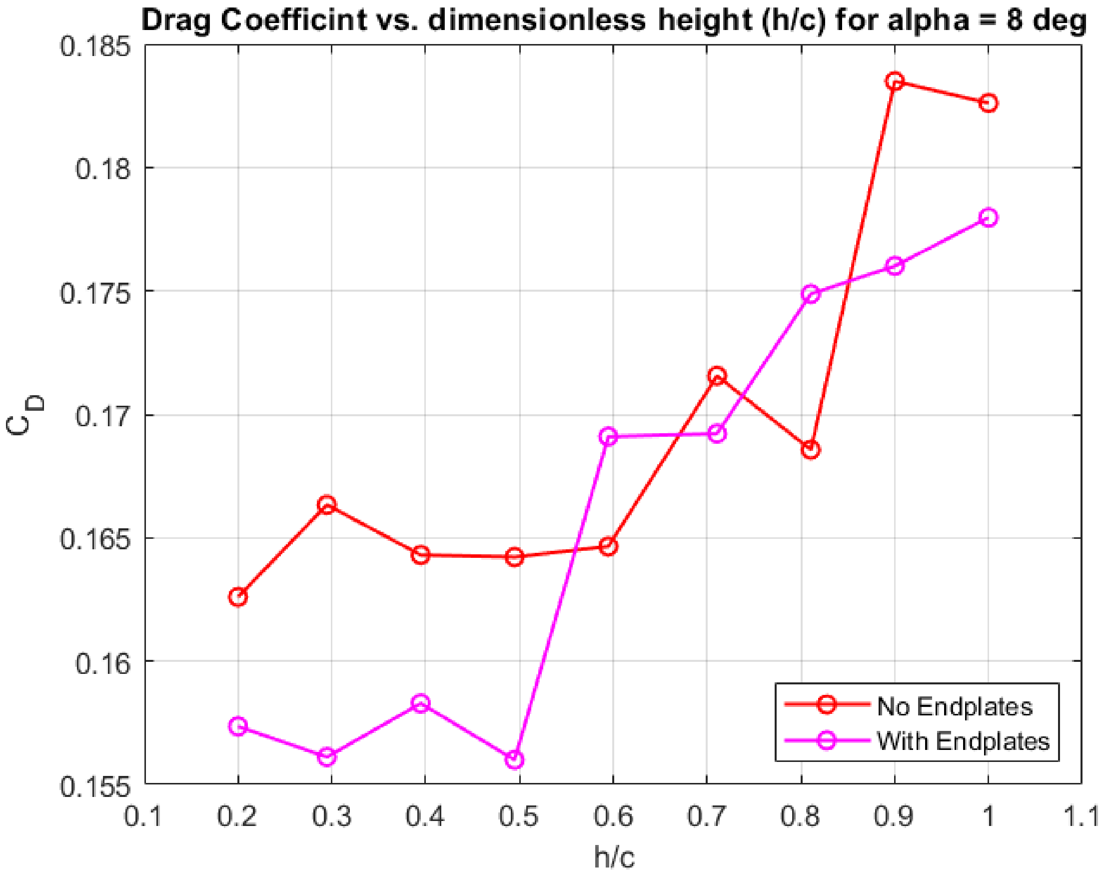

Source: The Author

theory/literature.

In order to evaluate an optimized relationship between the wing height in relation to the ground, a graph was made of the relationship between the downforce and the drag corresponding to their respective coefficients ($\left|\frac{C_L}{C_D}\right| \times h/c$) in Figure 39. It can be seen that the trend of the graph is very similar to that of Figure 37, which evaluates only the C_L, showing that, for a racing car, increasing the C_L is generally more important than reducing C_D. So much so that there is a big difference, both for the airfoil without endplates, and for the same one with endplates, from the $\left|\frac{C_L}{C_D}\right|$ from one height to another; referring that the most recommended height from the ground for the E423, subject to a flow velocity of 22 m/s and an angle of attack of 8° is $h \approx 56\ mm$ for the airfoil with endplates and $h \approx 75\ mm$ for it without this accessory. This also proved that the addition of endplates is indispensable for any of the conditions evaluated.

In relation to the XFRL5 graph (Figure 34d), a lower $\left|\frac{C_L}{C_D}\right| \times h/c$ ratio can be seen in general, for all heights. This comes from the fact that C_L is inherently reduced, as already explained in test 1, and also because C_D is increased by the hod.

"Because many race cars use front wings, typically mounted as close as h/c of

Figure 39 – $\left|\frac{C_L}{C_D}\right| \times h/c$ for the second test

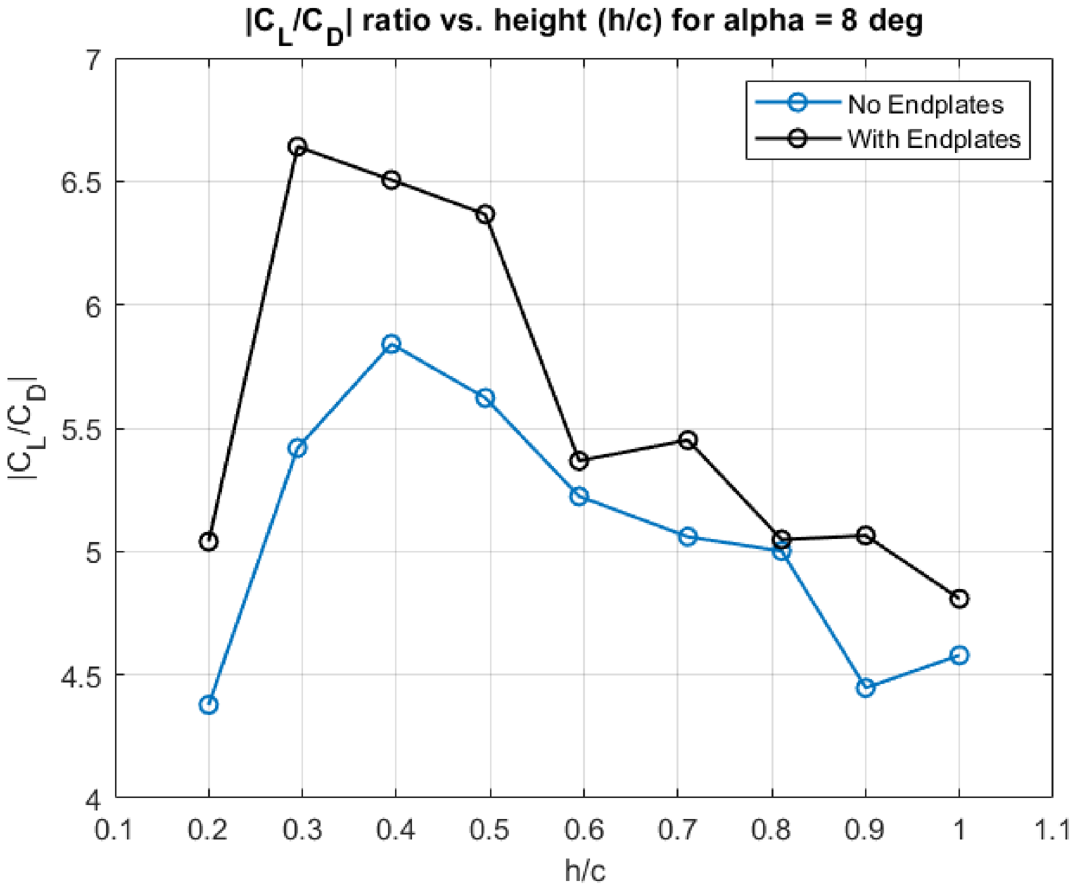

Source: The Author

0.1–0.3, this principle is clearly utilized in race car design" (KATZ, 2006). This quote said by Katz, can even be proven by the better relationship between C_L and C_D for the lowest values of h/c, which are the most relevant for a racing car and are the ones that suffer the most from the ground effect. however, without the viscous effects being predominant, thus without the wing being excessively close to the ground. This causes the phrase to be "corrected" for the E423 airfoil when it is subjected to a flow considered to be low Reynolds, changing to $0.2 < h/c < 0.4$, for the reasons already mentioned, especially the high camber of the E423 airfoil, which causes the dimensionless distance to be inherently "increased".

5.3.1 Possible sources of errors in the experiment

Like all purely experimental work, this one is subject to errors typical of works of this nature, which can be systematic or random.

The way the experiment sought to minimize part of the errors was to use the statistical principle of increasing the number of samples, by collecting for each condition around 900 measurements separated by a time interval of $0.2s$; and look for different equipment conditions, which, in the case of the wind tunnel, the 900 samples of each wing condition were divided into 3 cycles of turning the wind tunnel on and off, reducing the equipment error.

However, it is not possible to fully mitigate all sources of error, despite being able to control and predict them. The sources of error raised for this work are:

- **Uncertainty in Direct Quantities (presence of standard deviation)**: The repetition of a measurement of the variables (Lift and Drag) under the same experimental conditions leads to a random distribution of results around an average value (arithmetic mean), which can be considered as the best value obtained in this measure. However, a relatively high standard deviation is noted in the tables, this comes from the very sensitive nature of small disturbances in Fluid Mechanics, meaning that, even with a high number of samples, there are still uncertainties regarding the average values.
- **Test table vibrations:** the high speed and noise emission of the wind tunnel inherently causes the test table (seen as the "floor" in Figure 33) to vibrate; and since the aerodynamic balance is on the underside of this table, this vibration, therefore, may have affected its measurements.
- **Hole in the test table for fitting the rod and sheet metal:** The rod, as already mentioned, serves to connect the wing to the aerodynamic balance and transfer its force. In this way, the logic leads to the need to have a hole in the table of the same diameter as the rod. However, for smaller heights, the metal plate ends up being close to the table until it crosses it, which would only be possible by increasing the diameter of this hole. Thus, a small gap in the table well below the airfoil causes a slight modification in the behavior of the airflow in this region.
- **Variation in direction and magnitude of ambient wind speed:** Perhaps the most significant source of error, the fact that the tests take time and are carried out at different times of the day, makes the atmospheric wind conditions affect the results of the experiments, since the LAEX wind tunnel must have the flow of air thrown to the external environment; and when noticing Figure 33, the test bench is very close to the external environment and, therefore, subject to winds. This causes the random nature of natural winds to directly influence the measurements (see, for example, the drag measure outside the confidence interval of 14° and $h/c = 0.2$ for test 1).
- **Endplate "backrest" on test table for high α:** As already mentioned in the results, the

endplate had to be round at the front so that it would not touch the test table for low heights and high angles of attack. This not only limited the analysis on the difference between rectangular and round endplates (ALLEN, 2001), but also caused errors in measurements at low height.

- **Operator error for measurements and airfoil alignment:** The heights and angles of attack were measured with simple, analogue instruments, which always have a source of error. In addition, with each change in the airfoil condition, it had to be perfectly aligned in the three Cartesian axes for the perfect measurement, and this was done by the operator, who aligned the wing taking a horizontal line as a reference. This simple nature causes errors.

5.4 Visualization of air flow

In this section, the results obtained with the visualization of the flow using the wool yarn method (Tufts) will be presented with the model configured in the same position of the experiment with the aerodynamic balance. The configuration of this technique is very simple: just stick the pieces of wool in the characteristic regions of the wing with a little adhesive tape.

The intent of the flow visualization is primarily to see the nature of the flow different between the wing without endplates and with endplates, with both situations with the airfoil very close to the ground (under ground effect).

At one end of the wing, some pieces of wool were fixed: on the table (directly below the wing) and in regions of the wing tip.

From Figure 40, it is possible to perceive a flow with a larger vortex and a more "disorganized" flow for when the aircraft does not have endplates. This confirms both the theory and the results, as a lower induced drag was obtained for the wing with endplates.

Figure 40 – Visualization of flow at the tip of the airfoil

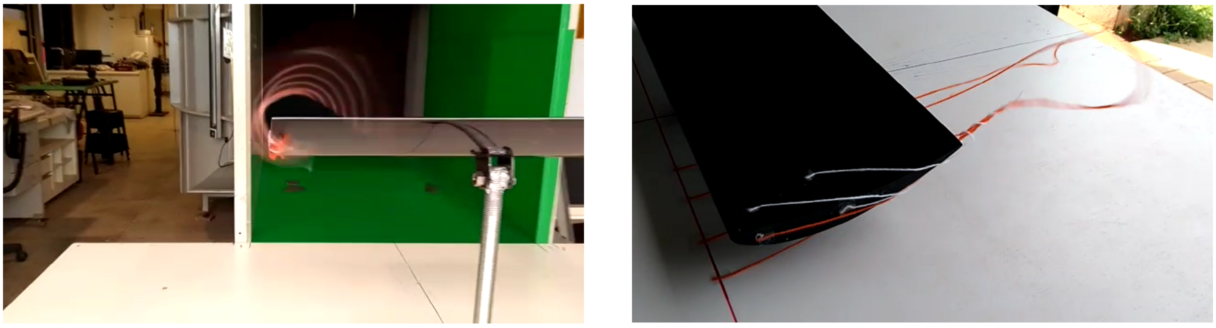

(a) Wing without endplates: rear view

(b) Wing without endplates: side view

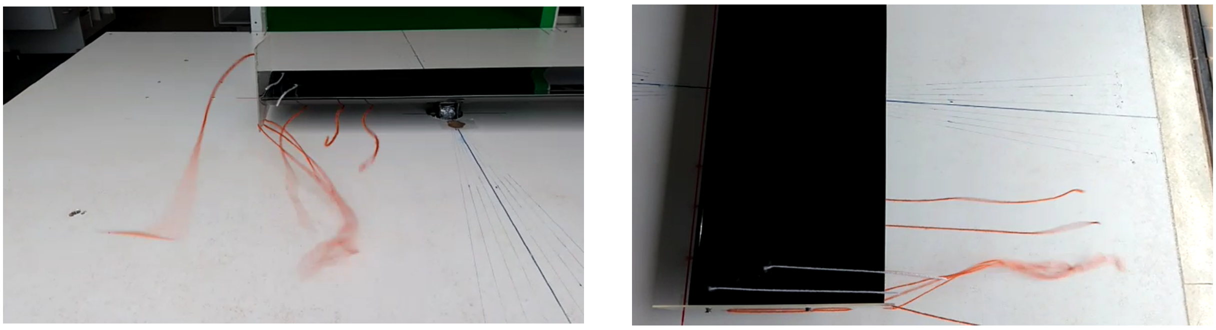

(c) Wing with endplates: rear view

(d) Wing with endplates: side view

Source: The Author

6 CONCLUSIONS

Race car wings are always close to the ground, making it necessary to evaluate the behavior of their wings in relation to their distance from the ground. And since the ground effect is, by definition, beneficial for the aerodynamic efficiency of the wing (except in values very close to the ground), it is recommended the quantitative study of its effects in relation not only to the height, but also to the angle of attack and the presence of endplates, as studied in this work. The main conclusion that can be drawn from the results of the experiment is that the airfoil should be close to the ground, but not too much (especially for the E423, which is an airfoil that is too arched). In addition, the presence of endplates is fundamental, due to the combination of simple geometry with a good increase in wing efficiency.

The setup of the experiment was a challenge from the beginning, especially to determine a method of variation of the height and the angle of attack, which were chosen the threaded rod and the arrangement of the sheet metal, respectively. However, this addition of physical parts in the experiment was the main cause of the increase in drag overall, especially at greater heights.

Explicitly, for test 1, C_L had its variation as a function of typical α for an airfoil in an ordinary situation (as in XFRL5) for $h/c = 1.5747$. However, a different behavior from the ordinary one was observed for $h/c = 0.2$, with a peak of C_L at 14° instead of 12° for the other height; contradicting the theory that the stall under ground effect occurs at smaller angles, evidencing the different behavior found for the angle 14° not only for C_D, but also for C_L.

As for test 2, the result was very consistent with the theory: for small distances ($h/c = 0,2$), the viscous effects were too predominant to produce enough downforce; however such effects end up with height increasing a little more, having a peak downforce of $28,2865\ N$ ($|C_{L_{max}}| = 1,0367$) for the wing with endplates and $26,1836\ N$ ($|C_{L_{max}}| = 0,9596$) for it without endplates. As for the drag, the behavior was not so consistent, in general due to the increase in the rod according to the height, interfering with the results; but interesting observations can be made: there is a very large jump in drag from $h/c = 0,5$ to $h/c = 0,6$, which can characterize the resurgence of vortices.

6.1 Suggestions for future work

A future work should evaluate the variation of the Reynolds number under the same conditions of this work, since the limitation of the speed and dimensions of the wind tunnel caused the Reynolds number to be an order of magnitude lower than usual for this category of wings; causing problems of viscous origin at high angles of attack for test 1. One should therefore make this assessment of how the nature of the Reynolds number affects this type of airfoil, focusing not only on the velocity of such airflow, but also on the proportions of this wing (which influence *Re* according to the equation 2.4). This Reynolds variation can be combined by analyzing the flow behavior more coldly for $0.1 < h/c < 0.5$, where the lowest drag ratio (especially induced drag) was observed with the highest values of downforce for the Reynolds number of this work ($Re = 267825$), and to verify if this behavior repeats itself when increasing the flow velocity or when increasing the size of the airfoil.

Another thesis suggestion would be to evaluate the different types and formats of endplates (ALLEN, 2001), since it was not possible to do this evaluation due to the fact that the endplate can touch the ground at high angles of attack at small heights. Both the size of the endplate and its shape should be evaluated, whether it is rounded or simply rectangular.

For a better visualization of the flow, to better evaluate the types of vortices, a more complex visualization, such as the use of smoke, can be done. In this way, one can, for example, raise theories of how the angle from 14° to $h/c = 0.2$ had such an unusual behavior compared to the rest of the measurements, being able to conclude a verdict if it was just a wrong measurement or some isolated behavior that can be predicted.

Another suggestion for future work is to evaluate this experimentation in a totally closed environment, immune to variations in atmospheric conditions, especially wind.

REFERENCES

ALLEN, K. R. Wing in ground effect vehicle with endplates. Spruson Ferguson, Level 35 St Martins Tower 31 Market Street, Sydney, NSW, p. 1–59, 2001.

ANDERSON, J. **Fundamentals of aerodynamics, 3. ed.** [S.l.]: McGraw-Hill, 2001.

BARLOW, J.; RAE, W. H.; POPE, A. **Low-speed wind tunnel testing. 3. ed.** [S.l.]: New York: Wiley, 1999.

E423 - Eppler E423 high lift airfoil. Available at: <http://airfoiltools.com/airfoil/details?airfoil=e423-il>. Accessed on: 14 jan. 2022.

FARON, H.; MARCINKOWSKI, W.; HAMIGA, W.; PRUSAK, D. The influence of aerodynamics forces on the steering characteristics of the car case study. Al. Mickiewicza, Cracow, Poland, 2015.

HUCHO, W.-H. **Aerodynamics of road vehicles: from fluid mechanics to vehicle engineering. 4. ed.** [S.l.]: Warrendale, PA : Society of Automotive Engineers, 1998.

INCROPERA, F.; DEWIT, D. **Fundamentals of Heat and Mass Transfer, 6 ed.** [S.l.]: College of Engineering. University of Notre Dame, 2007.

KATZ, J. **Race car aerodynamics: designing for speed 2. ed.** Cambridge, MA, USA, 2006. 27–63 p. Available at: <https://doi.org/10.1146/annurev.fluid.38.050304.092016>.

KNOWLES K.; DONOGHUE, D. F. M. A study of wings in ground effect. Loughborough University Conference on Vehicle Aerodynamics, v. 22, p. 1–11, 1994.

NAIR, P. **Aerodynamics - Formula SAE**. [s.n.], 2014–2015. Available at: <https://pt.slideshare.net/PreethiNair15/aerodynamics-formula-sae>. Accessed on: 18 jan. 2022.

PIOLA, G.; SOMERFIELD, M. **Análise técnica: Lotus 79 - como um erro ajudou a criar um ícone da F1**. 2020. Available at: <https://motorsport.uol.com.br/f1/news/analise-tecnica-lotus-79-como-um-erro-ajudou-a-criar-um-icone-da-f1/4795093/>. Accessed on: 01 jan. 2022.

RAYMER, D. P. **Aircraft design: A conceptual approach**. [S.l.]: AIAA education series, 1992.

SKYBRARY. **Theory of Flight: Ground Effect**. 2012. Article on published website. Available at: <https://skybrary.aero/articles/ground-effect>. Accessed on: 18 fev. 2022.

TANNEHILL, J. C.; ANDERSON, D. A.; PLATCHER, R. H. **Computational Fluid Mechanics and Heat Transfer, 2. ed.** [S.l.]: McGraw-Hill, 1984.

TOET W.; ZERIHAN, J. Z. X. Ground effect aerodynamics of race cars. Applied Mechanics Reviews, American Society of Mechanical Engineers, v. 59, p. 32–49, 2006. Available at: <https://doi.org/10.1115/1.2110263>.

WINSLOW J.; OTSUKA, H. G. B. C. I. Basic understanding of airfoil characteristics at low reynolds numbers. Journal of Aircraft, Reston (Virginia), v. 55, p. 1–12, 2017.

XFRL5, Theoretical background.

ZAHM A. F.; BEAR, R. Ground-plane influence on airplane wings. Journal of the Franklin Institute, Elsevier, v. 191, n. 5, p. 687–693, 1921. Available at: <https://doi.org/10.1016/S0016-0032(21)90176-5>.

ZERIHAN, J.; ZHANG, X. Aerodynamics of a single element wing in ground effect. University of Southampton, Southampton, England SO17 1HJ, United Kingdom, 2000. Available at: <https://doi.org/10.2514/6.2000-650>.

ZERIHAN, J. D. C. **An Investigation into the Aerodynamics of Wings in Ground Effect**. Master's Thesis (Master's Thesis) — School of Engineering Sciences, University of Southampton, Southampton, 2001.

GLOSSÁRIO

CAD Computer Aided Design

CFD Computational Fluid Dynamics

LAEX Experimental Aerodynamics Laboratory

APPENDIX A – TABLE WITH THE 3 MEASUREMENTS PERFORMED FOR PART 1 OF THE EXPERIMENT

Each average of each table of each test below was subjected to at least 900 measurements divided into 3 wind tunnel on/off cycles. For each cycle, the 300 measurements were taken in 60 seconds each. The average of each of these 3 sets of measurements, for the first part of test 1 ($h/c = 1.5747$), is shown in the tables below and also follows the figure of the distribution of one of them over the 60 seconds (more precisely set #1 for $h/c = 0°$).

Average of each of the three lift measurements for each angle of attack

	Lift Means	Standard Deviation
0°	[-3,929 -4,7576 -3,753]	[1,4996 1,2382 1,3302]
4°	[-13,733 -12,567 -13,525]	[1,5194 1,4826 1,1848]
8°	[-21,6811 -22,024 -21,521]	[1,3357 1,4583 1,2688]
12°	[-23,172 -26,367 -23,664]	[1,6779 1,3311 1,8639]
14°	[-21,371 -20,644 -22,622]	[1,0597 1,2439 1,6780]

Average of each of the three total drag measurements for each angle of attack

	Drag Means	Standard Deviation
0°	[6,3896 4,5339 4,1818]	[0,90383 0,8655 1,0342]
4°	[3,8118 3,0208 2,9069]	[0,9557 0,9470 0,41102]
8°	[3,9399 3,1384 3,5558]	[0,64655 0,84176 0,59148]
12°	[4,5809 5,1231 3,8413]	[0,82548 0,57099 0,95813]
14°	[5,7924 6,8885 6,4523]	[1,2377 0,89702 0,85964]

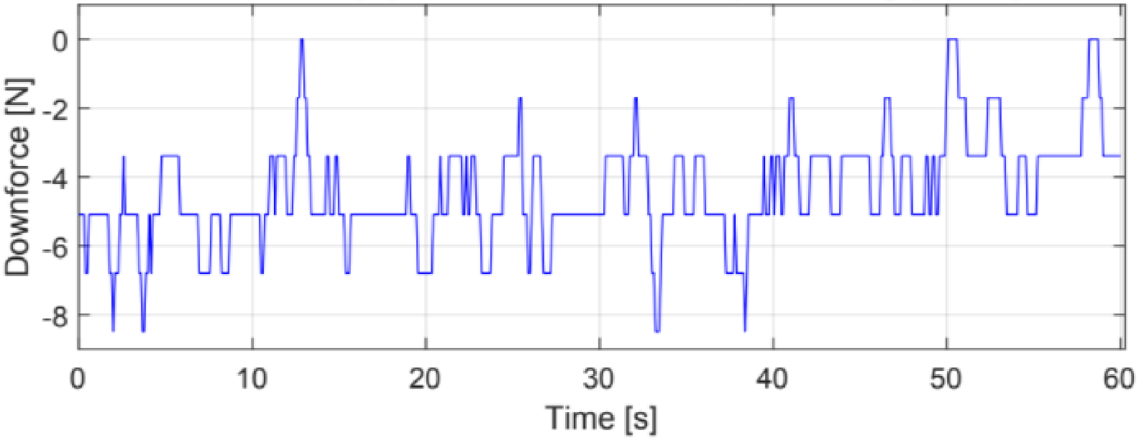

Downforce [N] for h = 300 mm and alpha = 0deg [Test 1]

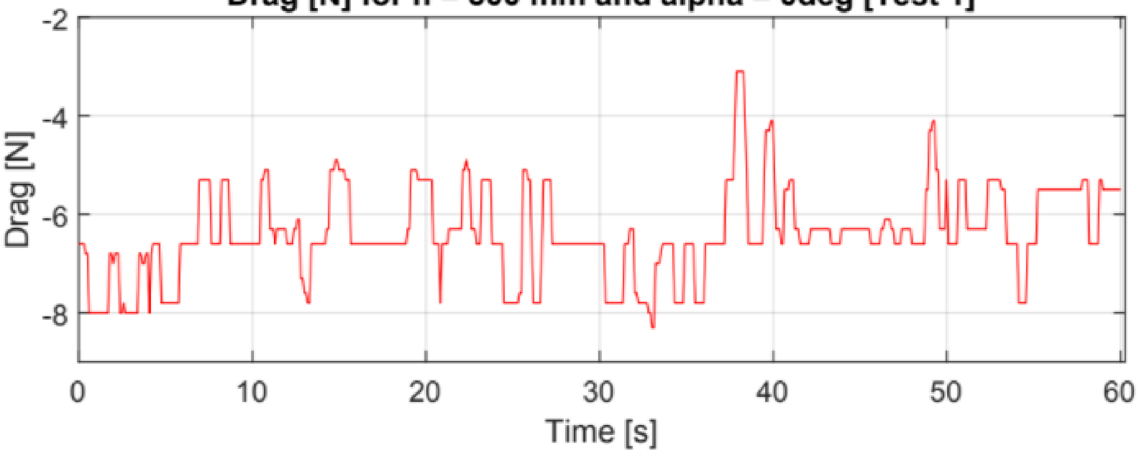

Drag [N] for h = 300 mm and alpha = 0deg [Test 1]

APPENDIX B – CORRECTIONS FOR TESTING IN WIND TUNNELS

B.0.1 Corrections

According to the wind tunnel book (BARLOW *et al.*, 1999), each wind tunnel has particularities that reasonably modify the input parameters of the relevant properties (such as flow velocity, laminarity/turbulence, etc.), since all the theory discussed in the theoretical foundation section of this report takes into account the conditions as being ideal, that is, without physical blockages, unbalances in calibrations or changes in flow lines. Nonetheless, for real-life experimentation, the wind tunnel will produce accuracy deviations, which are enumerated and explained in the following subsections.

B.0.1.1 The Solid Blockage

With constant testing in low-Reynolds wind tunnels (BARLOW *et al.*, 1999), it was identified that the presence of the inner walls in a wind tunnel causes a kind of confinement of the airflow around a model in the test section, reducing the area in which air flows compared to the air free of obstacles.

Evaluating the fundamental equations of fluid mechanics (2.1, 2.2 and 2.3) and also the basic principles of lift, such as the inverse relationship between pressure and velocity, it is verified that the air velocity increases as the air flows in the vicinity of the model, characterizing the effect called solid blocking. Mathematically, this effect is a function of the general geometry of the model in terms of its thickness and its distribution as the chord is traversed; however, the curvature of the model has a negligible influence on the effect.

$$\varepsilon_{sb} = \frac{\pi^2}{12}\,\lambda_2\left(\frac{t^2}{h_{wt}^2}\right) \tag{B.1}$$

Therefore, in the equation B.1, the correction factor (ε_{sb}) is deduced from it through the quadratic relationship between the maximum thickness of the airfoil (t) and the height of the wind tunnel (h_{wt}), related by a constant (λ_2) called Shape Factor that consists of a related geometric constant with the type of airfoil along with its thickness ratio ($\frac{t}{c}$).

For the E423 airfoil, its maximum thickness is 2.9 *mm*; the LAEX wind tunnel has a height of 60 cm. From the figure 41, which relates the Shape Factor with the types of airfoils, it can be concluded that $\lambda_2 \approx 1,2$

Figure 41 – Shape factors for selected forms

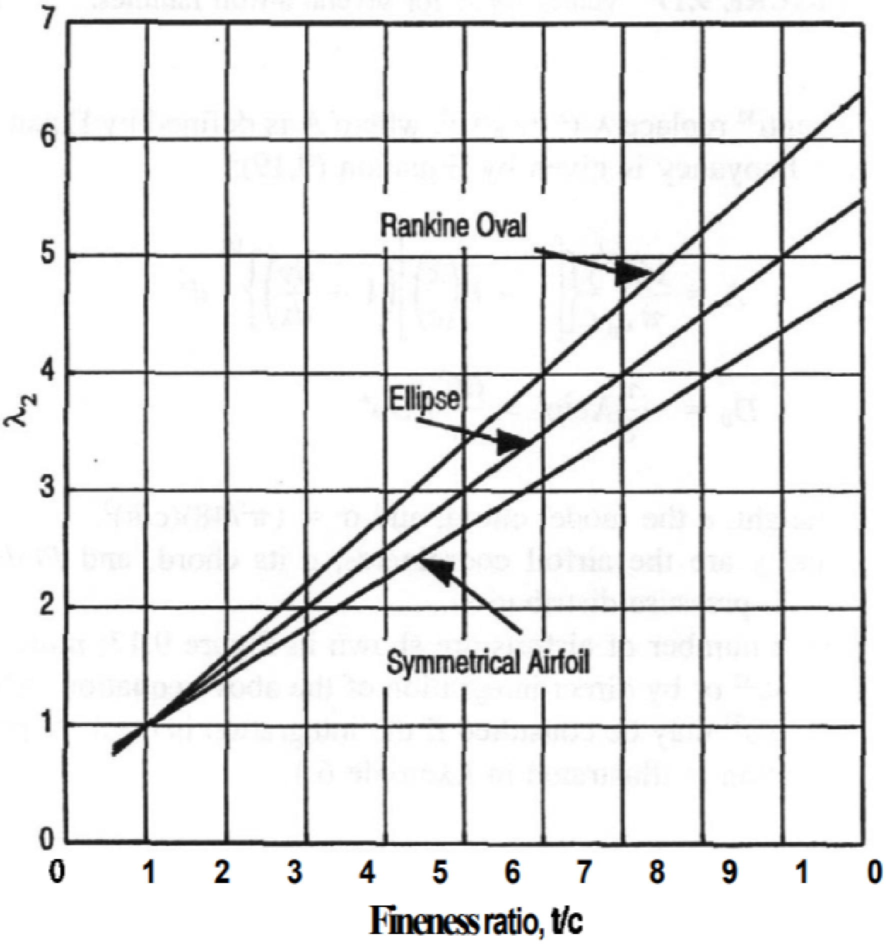

Source: (BARLOW *et al.*, 1999)

B.0.1.2 The Wake Blockage

Any real-solid body without any suction-type boundary layer control (such as vortex generators for the Magnus effect) generates in a wind tunnel test a wake that will have an average velocity lower than that same condition if it were under a free flow regime. According to the continuity principle (represented through the equation 2.1), the off-track velocity in a closed wind tunnel must therefore be greater than the free-flow velocity, so that a constant volume of fluid can pass through each crossing of the test section, respecting the mass conservation. The higher velocity in the main flow has, by equation (2.3), a reduced pressure, which generates a different pressure gradient that consequently will slightly increase the fluid velocity. Again, the limited height of the wind tunnel is the cause of this physical difference, which directly affects the drag behavior. The literature (BARLOW *et al.*, 1999), therefore, defines a new correction factor related to the wake blocking, as shown in equation B.2.

$$\varepsilon_{wb} = \frac{c}{2h_{wt}} C_{Du} \tag{B.2}$$

B.0.1.3 Streamline Curvature

The closed section of the wind tunnel means that the streamlines further away from the specimen do not produce the same curvature if it were in free air flow. This causes the apparent curvature of the flow to be slightly greater. Consequently, the airfoil in a closed wind tunnel has more lift and momentum about the ¼ chord position at a given angle of attack than it would in open air. The correction, symbolized by σ, is given by (BARLOW *et al.*, 1999):

$$\sigma = \frac{\pi^2}{48} \frac{c^2}{h_{wt}^2} \tag{B.3}$$

These three corrections apply in the evaluation of the fundamental numbers of the flow, such as the Reynolds number, whose correction is of percentage addition and is represented by the equation B.4; and the angle of attack, whose correction is represented by the equation B.5. Remembering that the sub-index "*u*" consists of the uncorrected property and the properties without it are the already corrected ones.

$$Re = Re_u(1 + \varepsilon_{sb} + \varepsilon_{wb}) \tag{B.4}$$

$$\alpha = \alpha_u + 8,55\sigma \left(C_{Lu} + 4C_{Mu\frac{1}{4}} \right) \tag{B.5}$$

There is also the necessary correction of momentum, lift and drag coefficients (equations B.6, B.7 and B.8, respectively), which use the same coefficients found for the angle of attack and the Reynolds number.

$$C_{M\frac{1}{4}} = C_{Mu\frac{1}{4}}[1 - 2(\varepsilon_{sb} + \varepsilon_{wb})] + \frac{1}{4}\sigma C_L \tag{B.6}$$

$$C_L = C_{Lu}[1 - \sigma - 2(\varepsilon_{sb} + \varepsilon_{wb})] \tag{B.7}$$

$$C_D = C_{Du}(1 - 3\varepsilon_{sb} - 2\varepsilon_{wb}) \tag{B.8}$$

APPENDIX C – TECHNICAL DRAWING OF THE FIXING PLATE

For the flange, follow the technical drawing made by SolidWorks with dimensions in millimeters.

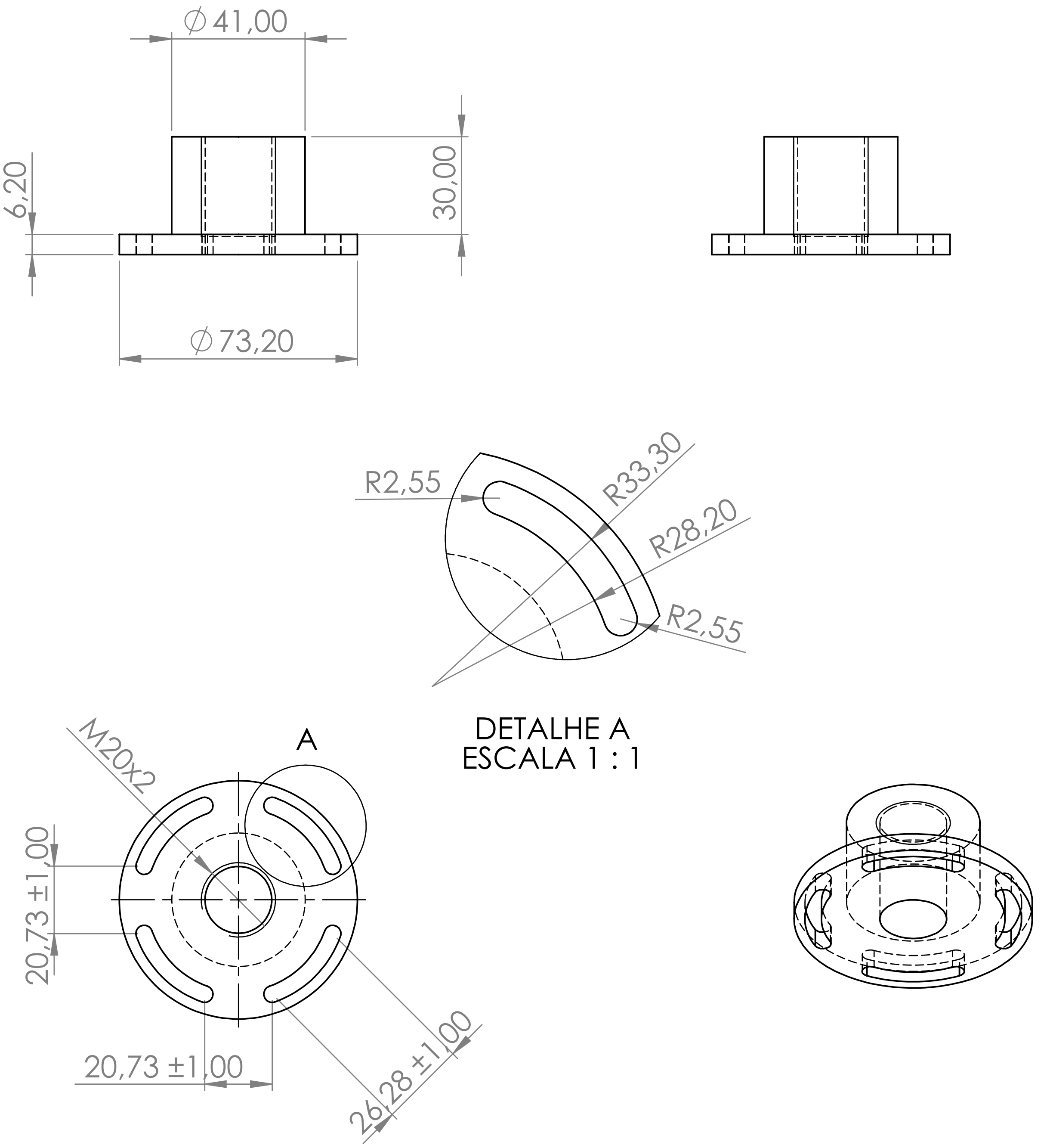

SE NÃO ESPECIFICADO:
DIMENSÕES EM MILÍMETROS
ACABAM. SUPERFÍCIE:
TOLERÂNCIAS:
LINEAR:
ANGULAR:

ACABAMENTO:

REBARBAR E QUEBRAR ARESTAS AGUDAS

NÃO MUDAR ESCALA DO DESENHO

REVISÃO

	NOME	ASSINATURA	DATA
DESEN.			
VERIF.			
APROV.			
MANUF.			
QUALID.			

TÍTULO:

MATERIAL:

DES. Nº

flange

A4

PESO:

ESCALA:1:2

FOLHA 1 DE 1

APPENDIX D – TECHNICAL DRAWING OF THE FIXING PLATE

For the fixing plate, follow the technical drawing made by SolidWorks with dimensions in millimeters.

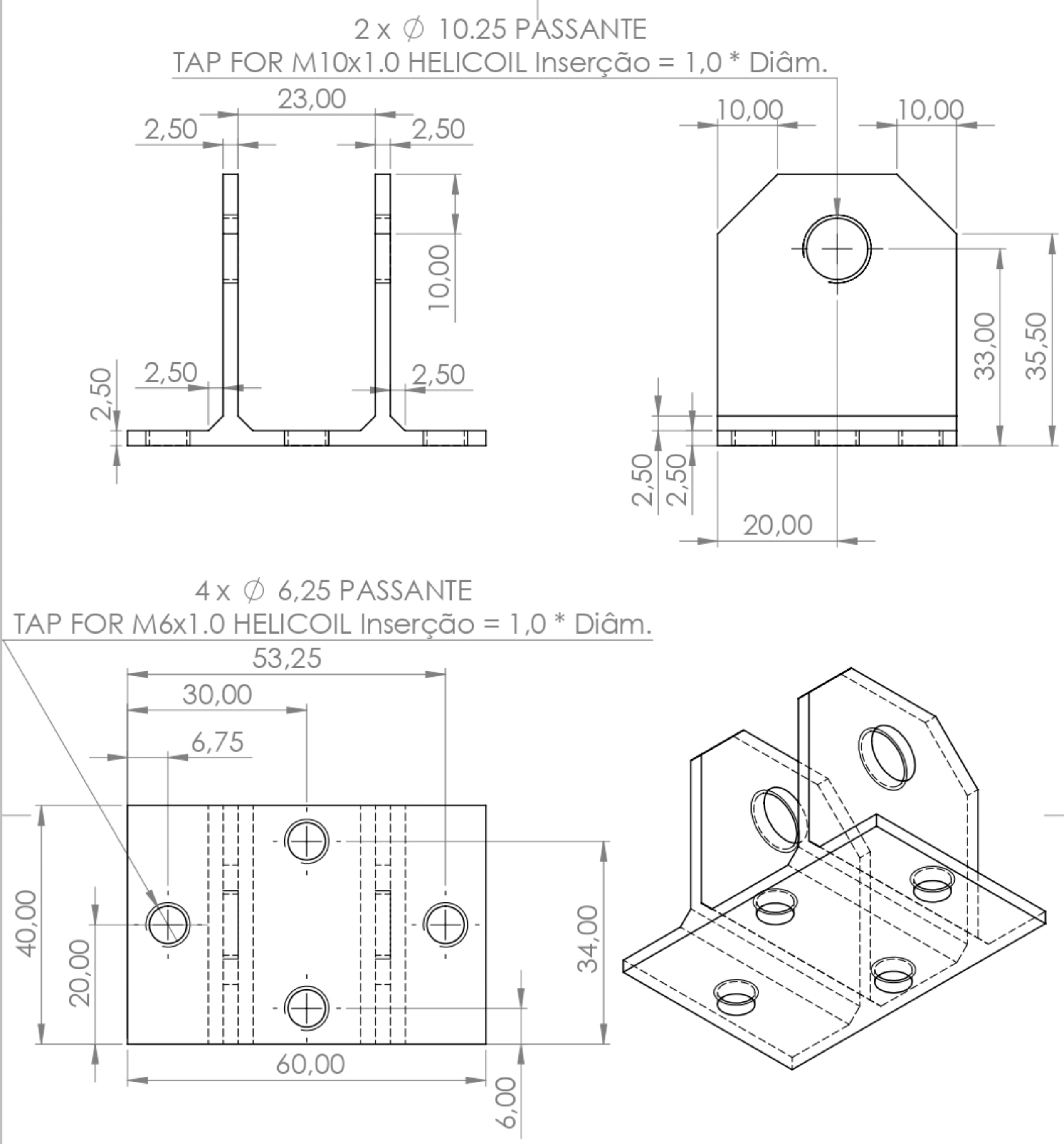

2 x ∅ 10.25 PASSANTE
TAP FOR M10x1.0 HELICOIL Inserção = 1,0 * Diâm.

4 x ∅ 6,25 PASSANTE
TAP FOR M6x1.0 HELICOIL Inserção = 1,0 * Diâm.

SE NÃO ESPECIFICADO:
DIMENSÕES EM MILÍMETROS
ACABAM. SUPERFÍCIE:
TOLERÂNCIAS:
LINEAR:
ANGULAR:

ACABAMENTO:

REBARBAR E
QUEBRAR
ARESTAS
AGUDAS

NÃO MUDAR ESCALA DO DESENHO

REVISÃO

	NOME	ASSINATURA	DATA
DESEN.			
VERIF.			
APROV.			
MANUF			
QUALID			

TÍTULO:

MATERIAL:

PESO:

DES. Nº

Chapa de Fixação

A4

ESCALA:1:1

FOLHA 1 DE 1